

Magnetic-Field Universality of the Kondo Effect Revealed by Thermocurrent Spectroscopy

Chunwei Hsu,¹ Theo A. Costi,^{2,3} David Vogel,⁴ Christina Wegeberg,⁴
Marcel Mayor,^{4,5,6} Herre S.J. van der Zant,¹ and Pascal Gehring^{1,7,*}

¹*Kavli Institute of Nanoscience, Delft University of Technology, Lorentzweg 1, Delft 2628 CJ, The Netherlands*

²*Peter Grünberg Institut, Forschungszentrum Jülich, 52425 Jülich, Germany*

³*Institute for Advanced Simulation, Forschungszentrum Jülich, 52425 Jülich, Germany*

⁴*Department of Chemistry, University of Basel, St. Johannis-Ring 19, 4056 Basel, Switzerland*

⁵*Institute for Nanotechnology (INT), Karlsruhe Institute of Technology (KIT), P.O. Box 3640, 76021 Karlsruhe, Germany*

⁶*Lehn Institute of Functional Materials (LIFM), School of Chemistry,
Sun Yat-Sen University (SYSU), 510275 Guangzhou, China*

⁷*IMCN/NAPS, Université Catholique de Louvain (UCLouvain), 1348 Louvain-la-Neuve, Belgium*
(Dated: April 12, 2022)

Probing the universal low-temperature magnetic-field scaling of Kondo-correlated quantum dots via electrical conductance has proved to be experimentally challenging. Here, we show how to probe this in nonlinear thermocurrent spectroscopy applied to a molecular quantum dot in the Kondo regime. Our results demonstrate that the bias-dependent thermocurrent is a sensitive probe of universal Kondo physics, directly measures the splitting of the Kondo resonance in a magnetic field, and opens up possibilities for investigating nanosystems far from thermal and electrical equilibrium.

Introduction.— The Kondo effect, originally describing the anomalous increase with decreasing temperature in the resistivity of nonmagnetic metals containing a small concentration of magnetic impurities [1–3], is now a ubiquitous phenomenon in physics, forming the starting point for understanding the Mott transition [4], heavy fermions [5], and transport through correlated nanostructures, such as quantum dots [6, 7], molecules [8] and adatoms on surfaces [9]. In the so-called “QCD Kondo effect” [10], it also constitutes one of the first known examples of asymptotic freedom [11, 12], a property of the strong interaction in particle physics.

A key feature of the Kondo effect is its universality [13–15]. For example, the temperature dependence of the linear conductance $G(T)$ of a spin-1/2 quantum dot is described by a unique universal scaling function $G(T)/G(0) = g(T/T_K)$ of T/T_K , where T is the temperature and T_K is the Kondo scale, and is used as a hallmark for establishing a spin-1/2 Kondo effect in quantum dot systems [16]. The same holds for exotic realizations of the Kondo effect [17–20], with each having its own characteristic set of universal scaling functions. Thus, universality in Kondo systems provides hallmarks for identifying the particular Kondo effect in a given experiment [18, 19, 21].

In this Letter, we address another aspect of universality of Kondo-correlated quantum dots, namely the universal magnetic-field scaling in the low-temperature ($T \ll T_K$) Fermi-liquid regime of quantum dots. While our interest is in the thermocurrent, we first specify what we mean by low-temperature magnetic field scaling in the context of the more familiar differential conductance $G(T, V_{sd}) = dI/dV_{sd}$ (derivative of the electrical current with respect to source-drain voltage). Specifically, for the asymmetrically coupled quantum dot device investigated in this Letter [Fig. 1(b)], described within the Ander-

son impurity model [Fig. 1(c)], $G(T \ll T_K, V_{sd} \ll T_K)$ is given, for *arbitrary* magnetic fields B , within higher-order Fermi liquid theory [22–24] as

$$\frac{dI}{dV_{sd}} \propto a_0 - c_T \left(\frac{\pi T}{T_K} \right)^2 - c \frac{V_{sd}}{T_K} - c_V \left(\frac{V_{sd}}{T_K} \right)^2, \quad (1)$$

with field-dependent coefficients a_0, c_T, c and c_V [25]. The low-temperature magnetic-field scaling that we refer to is reflected in the universal dependence of the curvature coefficients $c_V(B) \propto -\partial^2 G / \partial V_{sd}^2$ and $c_T(B) \propto -\partial^2 G / \partial T^2$ on B/T_K in the Kondo regime [22–24] [26]. Surprisingly, the exact dependence of c_V and c_T on magnetic field has only recently been calculated via a generalization of Nozières Fermi-liquid theory [27] to nonequilibrium and particle-hole asymmetric situations [22–24]. The results show that c_V and c_T are universal functions of magnetic field which change sign at a universal crossover field $B = B_c$ describing the onset of the splitting of the Kondo resonance in dI/dV_{sd} , in agreement with predictions for B_c for the Kondo model [28]. Nevertheless, establishing this universality and the splitting of the Kondo resonance in dI/dV_{sd} is intrinsically difficult [29–32]. Yet, both serve as useful experimental hallmarks of the Kondo effect in quantum dots.

Here, we propose a different approach to address magnetic-field scaling in the strong-coupling Kondo regime of quantum dots by employing the recently developed thermocurrent spectroscopy [37]. We experimentally show that the thermocurrent, I_{th} , of a molecular quantum dot in the Kondo regime exhibits a clear feature as a function of magnetic field, in the form of a zero-bias ($V_{sd} = 0$) kink appearing for fields B larger than a certain value, which we denote by B_{th} . We explain this behavior within higher-order Fermi-liquid theory [22, 24] for $V_{sd} \ll T_K$, and an approximate nonequilibrium Green

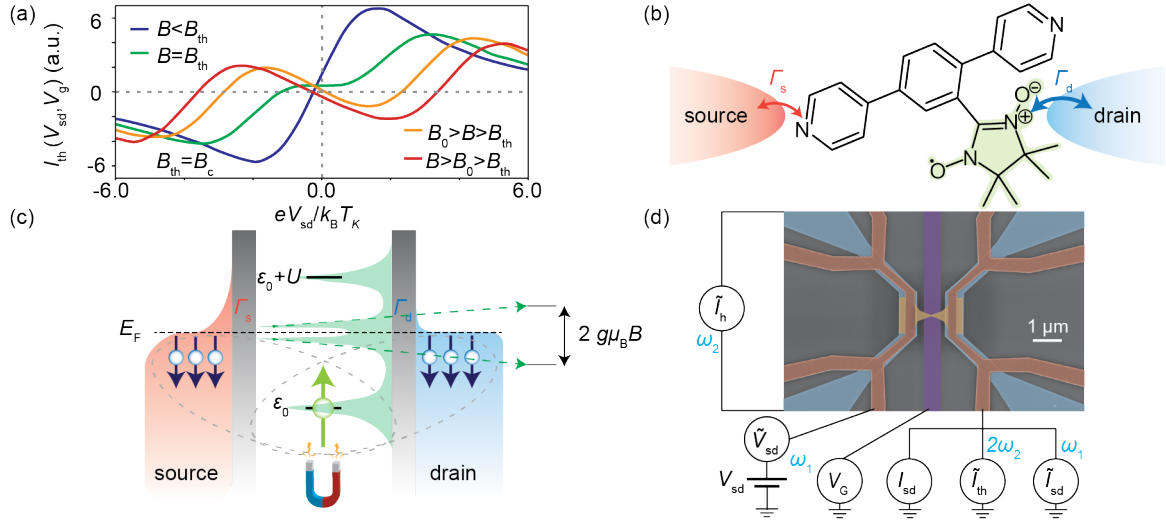


Fig. 1. (a) Sketch of I_{th} vs V_{sd} in the Kondo regime for several B . $(\partial I_{th}/\partial V_{sd})|_{V_{sd}=0}$ is a universal function of B/T_K and changes sign (“kink”) at a universal field $B = B_{th} = B_c$ [Fig. 4(a)], while $I_{th}(V_{sd} = 0)$ [33] changes sign at $B = B_0 > B_c$ and is nonuniversal [Fig. 4(a), Ref. 34 and Sec. SM.3.5.5 [25]]. (b) Molecular junction of a NNR molecule anchored to source and drain leads. (c) Anderson model of (b) in a magnetic field B . A singly occupied level ϵ_0 with Coulomb repulsion U and gate voltage $V_g = (\epsilon_0 + U/2)/\Gamma$ coupled to hot and cold source and drain leads with strength $\Gamma = \Gamma_s + \Gamma_d$ gives rise to a spin-1/2 Kondo effect for $V_g \approx 0$ resulting in a Kondo resonance at the Fermi energy, E_F . The field B splits the up and down levels at ϵ_0 by $g\mu_B B$ and the Kondo resonance in dI/dV_{sd} by $2g\mu_B B$ [35, 36] (for $g\mu_B B \gg k_B T_K$). A thermal bias $\Delta T > 0$ causes a thermocurrent I_{th} to flow between source and drain, measured as described in (d). (d) False-coloured scanning electron microscopy image of the thermoelectric device. Bias and thermal voltages are generated by a DC+AC bias voltage source, $V_{sd} + \tilde{V}_{sd}(\omega_1)$, and a AC heater current source, $\tilde{I}_h(\omega_2)$, on the hot left lead. The resulting DC, AC electrical currents and AC thermocurrent, I_{sd} , $\tilde{I}_{sd}(\omega_1)$ and $\tilde{I}_{th}(2\omega_2)$, are measured simultaneously on the cold right lead.

function approach [38] for $V_{sd} \gtrsim T_K$. Within the former, to leading order in V_{sd}, T and ΔT , where ΔT is the applied thermal-bias, we find in the low-temperature strong-coupling regime $\Delta T \ll T \ll T_K$,

$$I_{th}(T, V_{sd}) = \gamma \frac{\pi^2 k_B^2}{3} T \Delta T [s_0(B) + s_1(B) V_{sd}], \quad (2)$$

with constant γ and coefficients $s_0(B)$ and $s_1(B)$ [25]. Remarkably, we show that, (i), $s_1(B)/s_1(0)$ and $c_V(B)/c_V(0)$ are described by essentially the same universal scaling function in the Kondo regime, showing that $\frac{dI_{th}}{dV_{sd}}|_{V_{sd}=0} [\propto s_1(B)]$ probes magnetic field universality, and, (ii), B_{th} coincides with B_c , thus demonstrating that thermocurrent spectroscopy provides a new route to directly probe the splitting of the Kondo resonance [28] and extract the universal field $B_c = B_{th}$. Our findings are concisely summarized in the sketch in Fig. 1(a). We note, that in contrast to the zero-bias thermocurrent slope, the zero-bias thermocurrent, $I_{th}(T, V_{sd} = 0) [\propto s_0(B)]$, measured in Ref. 33 as a function of gate-voltage (V_g) and magnetic field and found to change sign at a certain field B_0 , is nonuniversal [Fig. 4(a), Ref. 34 and Sec. SM.3.5.5 [25]]. Thus $I_{th}(T, V_{sd} = 0)$ does not provide a hallmark for the splitting of the Kondo resonance and cannot be used to extract B_c , in contrast to the thermocurrent spectroscopy proposed in this Letter.

Experiment and results.— The experiment is carried

out on a molecular quantum dot consisting of an organic radical molecule (nitronyl nitroxide radical, NNR) made up of a backbone and a nitronyl-nitroxide side group where an unpaired electron resides as shown in Fig. 1(b). Such free radical molecules are model systems to study the spin-1/2 Kondo effect [Fig. 1(c)] [39–41]. Furthermore, their asymmetric structure and the additional pyridine anchoring sites allow us to achieve asymmetric and strong coupling between the source/drain leads and the molecule (quantified by couplings Γ_s and Γ_d , Fig 1(b)). We form a NNR-molecule quantum dot in the thermoelectric device shown in Fig. 1(d) by immersing electromigrated nanogaps in the molecular solution [42]. The thermoelectric device incorporates a local backgate and two microheaters in direct thermal contact with the source/drain leads [see Fig. 1(d) and Sec. SM.1.1 [25]].

Evidence for a Kondo effect is shown by the strong suppression of the zero-bias peak in the measured dI/dV_{sd} , both as a function of increasing T [Figs. 2(a)-2(b)] and B [Figs. 2(c)-2(d)]. The T -dependence of the zero-bias peak height [Fig. 2(b)] is well described by the numerical renormalization group (NRG) conductance of a spin-1/2 Kondo model and yields $T_K = 12.8$ K (Sec. SM.1.3 [25]). Based on the structure of the molecule, an asymmetric coupling is expected. Assuming, $\Gamma_d \gg \Gamma_s$ (see Sec. SM.3.5.3 [25] for $\Gamma_d \ll \Gamma_s$), we find $\Gamma_s/\Gamma_d \approx 0.017$.

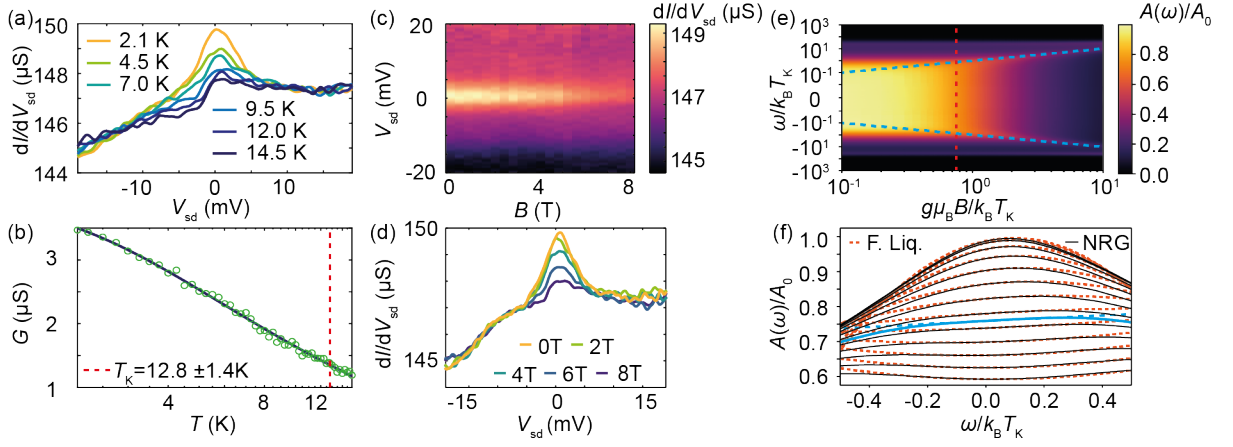


Fig. 2. (a) dI/dV_{sd} , of the molecular quantum dot vs V_{sd} at different temperatures. (b) Peak conductance of Kondo resonance vs temperature and fit to a spin-1/2 Kondo model yielding $T_K \approx 12.8$ K, see Secs. SM.1.3 and SM.2.3. (c)-(d) dI/dV_{sd} vs V_{sd} at different magnetic fields. (e) NRG Spectral function $A(\omega)/A_0$ with $A_0 = 1/2\pi\Gamma$ of the Anderson model vs energy (ω) and magnetic field for $V_g = (\varepsilon_0 + U/2)/\Gamma = -1$ and $U/\Gamma = 8$. Vertical dashed line: splitting field $B_c = 0.75k_B T_K/g\mu_B$. Blue dashed lines: positions $[\omega(B) = \pm g\mu_B B]$ of the split Kondo peaks in $A(\omega)$ for $B \gg B_c$ [35, 36]. (f) $A(\omega)/A_0$ from line cuts in (e) at $g\mu_B B/k_B T_K = 0, 0.1, \dots, 0.7, 0.75, 0.8, \dots, 1.2$ (solid lines), compared to $A(\omega)/A_0$ from Fermi-liquid theory (dashed lines). Blue lines: $B = B_c$. A g factor of $g = 2$ is used, as measured by electron paramagnetic resonance (Sec. SM.4.2 [25]).

An underscreened Kondo effect [18, 19], requiring a larger molecular spin ($S > 1/2$), is excluded, since such an effect results in a split Kondo resonance in dI/dV_{sd} starting already at zero field, which is not observed in Figs. 2(c)-2(d). Thus, a single-level Anderson model describing a $S = 1/2$ Kondo effect [Fig. 1(c)] is justified by the data. In the remainder of this Letter, the base temperature is kept at $T \approx 2$ K $\ll T_K$ while the thermocurrent is measured for a small thermal bias $\Delta T \approx 0.6$ K $\ll T \ll T_K$ so that we probe the strongly-coupled Kondo regime (see Secs. SM.2.4-5 and Secs. SM.3.6.4-5 [25] for thermal bias and temperature effects).

A closer look at the field dependence of dI/dV_{sd} in Figs. 2(c)-2(d), indicates that the expected splitting of the Kondo peak at $B_c \approx 7.15$ T [43] is not observed. This is in part due to a large non-Kondo (field and temperature independent) contribution in Figs. 2(a) and 2(d) which may mask the appearance of a splitting at zero bias. In addition, the largest field used, $B = 8$ T, was only marginally larger than B_c . For a device where higher fields relative to B_c could be applied, such a splitting is observed (Sec. SM.2.1 [25]). Despite these complications in extracting B_c from dI/dV_{sd} for the device studied, there is also a general problem in doing so, which can be appreciated by attempting this from exact theoretical results. This is illustrated in Figs. 2(e)-2(f) which show the spectral function $A(\omega = eV_{sd}) \sim dI/dV_{sd}$ within the NRG method and within Fermi-liquid theory. While the precise value of B_c is impossible to determine visually in Fig. 2(e) (vertical dashed line), it can be deduced from the line cuts in Fig. 2(f) as the field where the curvature of $A(\omega)$ vanishes. However, such accuracy in second derivatives of $A(\omega = eV_{sd}) \sim dI/dV_{sd}$ is difficult to attain

from experimental data with finite error bars.

Thermocurrent spectroscopy resolves the above difficulty. Figures 3(a)-3(b) show the measured thermocurrent versus bias voltage and magnetic field, while Figs. 3(c)-3(d) show analogous theory results within an approximate nonequilibrium Green function approach (Sec. SM.3.6 [25]). First, notice that the large non-Kondo contribution to the differential conductance [Figs. 2(a) and 2(d)], is absent in the thermocurrent Fig. 3(b), with the latter being largely symmetric in magnitude around zero bias, in agreement with theory [Fig. 3(d)]. This is because the thermocurrent effectively measures a difference of electrical currents (in the presence or absence of thermal bias), and thus filters out the non-Kondo contributions. By the same token the thermocurrent therefore probes universal aspects of Kondo physics more precisely than the differential conductance. Second, we now see a clear feature, in the form of a zero-bias kink with a negative slope of the thermocurrent, appearing in I_{th} at a field $B = B_{th}$. This is qualitatively captured, together with the behavior at $V_{sd} \gtrsim T_K$, by the approximate approach [Figs. 3(c) and 3(d)]. However, the precise field at which this feature occurs and its connection to B_c requires a more exact theory, which is provided by the higher-order Fermi-liquid theory [Eq. (2) and Sec. SM.3.5 [25]]. Preempting the result of this theory, we note that analyzing the experimental data in Figs. 3(a) and 3(b) for the slope of the thermocurrent $dI_{th}/dV_{sd}(V_{sd} = 0)$ at zero-bias voltage as a function of magnetic field, we find that this slope vanishes (i.e., the kink appears) at $B_{th} \approx 6.6$ T. This value is within 10% of the expected $B_c \approx 7.15$ T and already suggests that $B_{th} = B_c$, and, hence, that the splitting of the Kondo resonance can be directly mea-

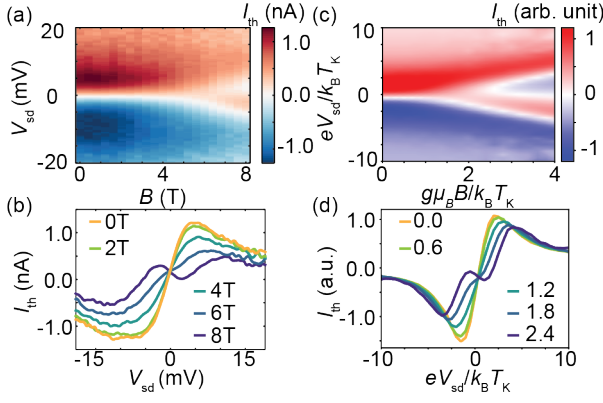


Fig. 3. (a)-(b) Measured I_{th} , vs V_{sd} at different magnetic fields. (c)-(d) Calculated I_{th} vs V_{sd} at different magnetic fields $g\mu_B B/k_B T_K$ for the Anderson model in Fig. 1(c) with $V_g = -2.5$, $U/\Gamma = 8$, $\Delta T/T_K = 0.2$ and $T/T_K = 0.5$.

sured in the bias voltage dependence of $I_{th}(V_{sd})$.

Equation (2), with $s_i(B)$, $i = 0, 1$ evaluated exactly for all B within the NRG (Sec. SM.3.5 [25]), allows us to address the experimentally observed sign change of $(\partial I_{th}(V)/\partial V_{sd})_{V=0} \propto s_1(B)$ upon increasing B above B_{th} (the “kink”) and to extract B_{th} . Figure 4(a) shows the normalized zero-bias thermocurrent slope $\propto s_1(B)/s_1(0)$, the normalized zero-bias thermocurrent $\propto s_0(B)/s_0(0)$ and the normalized curvature coefficient $\propto c_V(B)/c_V(0)$ as a function of B and for a range of V_g in the Kondo regime. First, notice that both $c_V(B)/c_V(0)$ and $s_1(B)/s_1(0)$ [in contrast to $s_0(B)/s_0(0)$] are universal scaling functions of $g\mu_B B/k_B T_K$ with only a weak dependence on V_g [inset Fig. 4(a)], and while distinct, they lie within about 1% of each other [inset Fig. 4(a) and Fig. S13 [25]]. Thus, measuring the field dependence of $s_1(B)$ via thermocurrent spectroscopy, requiring only a first derivative with respect to bias voltage, equivalently probes the magnetic-field universality from an electrical conductance measurement, which, however, requires a second derivative with respect to bias voltage and is consequently less accurate. Furthermore, since both $s_1(B)$ and $c_V(B)$ change sign at the same magnetic field, i.e., $B_{th} = B_c \approx 0.75k_B T_K/\mu_B$, thermocurrent measurements of Kondo correlated quantum dots at finite bias voltage provide a new way to determine the splitting of the Kondo resonance via a sign change in the slope of the thermocurrent with respect to bias voltage.

In Fig. 4(b) we show a direct comparison between theory and experiment for the slope of the zero-bias thermocurrent as a function of magnetic field. The experimental data follows well the universal curve for $s_1(B)/s_1(0)$, and the aforementioned value extracted from this data for $B_{th} \approx 6.6$ T ($g\mu_B B_{th}/k_B T_K = 0.69$), is consistent with the expected splitting field of $B_{th} \approx 7.15$ T ($g\mu_B B_{th}/k_B T_K \approx 0.75$). The largest available field, 8 T, did not allow accessing the minimum of the

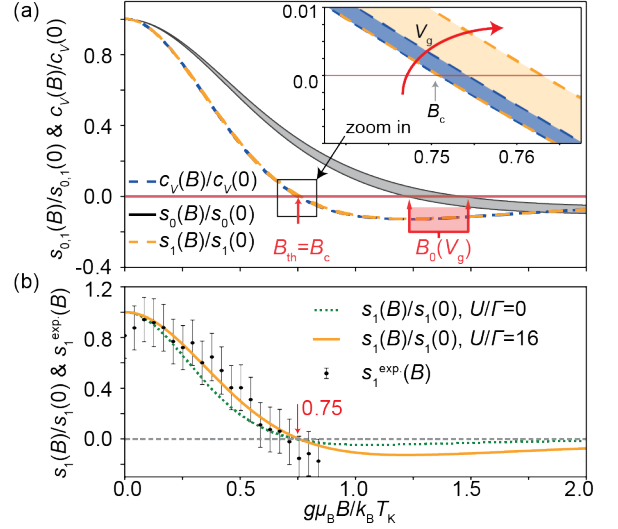


Fig. 4. (a) Normalized zero-bias thermocurrent slope $s_1(B)/s_1(0)$ and curvature coefficient $c_V(B)/c_V(0)$ vs $g\mu_B B/k_B T_K$, for gate voltages $1 \leq V_g = (\varepsilon_0 + U/2)/\Gamma \leq 5$ in the Kondo regime exhibiting scaling collapse [Anderson model in Fig. 1(c) with $U/\Gamma = 16$]. Also shown is the nonuniversal normalized zero-bias thermocurrent $s_0(B)/s_0(0)$ with a sign change at a strongly V_g -dependent B_0 . Inset: $c_V(B)/c_V(0)$ and $s_1(B)/s_1(0)$ in the region around $B = B_{th} = B_c \approx 0.75k_B T_K/g\mu_B$, and their V_g -dependence. (b) Least-squares fit of the experimental zero-bias thermocurrent slope $s_1^{exp}(B)$ to the universal curve for $s_1(B)/s_1(0)$. Error bars denote 1σ confidence intervals (see Sec. SM.1.4 [25]). A fit to the non-interacting case with $U = 0$ and $\varepsilon_0 = -0.1\Gamma$ (green dotted line) yielded an RMS deviation that was 194% larger than for the Kondo scaling curve. The estimated experimental $B_{th} \approx 0.69k_B T_K/g\mu_B$ is close to theory ($0.75k_B T_K/g\mu_B$).

$s_1(B)$ vs B curve or the slow increase of $s_1(B)$ to zero at $B \gg T_K$. The agreement between theory and experiment at the largest fields measured $B > B_{th}$ is reduced, but still within the error bounds of the experimental data. The extracted $B_c = B_{th}$ from the thermocurrent validates the theory prediction with higher accuracy than has so far been reported (see Sec. SM.3.5.2 [25]). The large energy level separation in a molecular quantum dot grants the observed good agreement between the theory and experiment, even under a simple single-level assumption in the transport window [Fig. 1(c)].

Conclusion.— In summary, we have studied the effect of a magnetic field on a Kondo-correlated molecular quantum dot via nonlinear thermocurrent spectroscopy. We demonstrated theoretically and confirmed experimentally, that the nonequilibrium thermocurrent, via its zero-bias slope $s_1(B)$, exhibits universal Fermi-liquid magnetic-field scaling, and that the vanishing of $s_1(B)$ at $B = B_{th}$ with $B_{th} = B_c$, directly probes the splitting of the Kondo resonance. Since the thermocurrent is largely robust against parasitic conductive phenomena, it provides a more clear cut signature of this hallmark than is

available from conductance measurements only. The ability to tune thermal and voltage bias, as well as temperature and magnetic field, opens up possibilities for using thermocurrent spectroscopy to yield insights into Kondo physics of nanoscale systems and may prompt theoretical investigations to address the largely unexplored area of nanosystems far from thermal and electrical equilibrium.

We thank J. de Bruijkere for his support in analysis software and M. van der Star for his help in sample fabrication. This work is part of The Netherlands Organization for Scientific Research (NWO). P.G. acknowledges financial support from the F.R.S.-FNRS of Belgium and a Marie Skłodowska-Curie Individual Fellowship under Grant TherSpinMol (ID: 748642) from the EU's Horizon 2020 research and innovation programme. H.S.J.v.d.Z., C.H., M.M. and D.V. acknowledge funding by the EU (FET-767187-QuIET). Computing time granted through JARA on the supercomputer JURECA at Forschungszentrum Jülich is gratefully acknowledged (T.A.C.). M.M. acknowledges support from the Swiss National Science Foundation (SNF grant numbers 200020-178808) and the 111 project (90002-18011002). C.W. thanks the Independent Research Fund Denmark for an international postdoctoral grant (9059-00003B).

* Email: pascal.gehring@uclouvain.be

- [1] W. J. de Haas, J. de Boer, and G. J. van den Berg, *Physica* **1**, 1115 (1934).
- [2] J. Kondo, *Prog. Theor. Phys.* **32**, 37 (1964).
- [3] A. C. Hewson, *The Kondo Problem to Heavy Fermions* (Cambridge University Press, Cambridge, 1997).
- [4] A. Georges, G. Kotliar, W. Krauth, and M. J. Rozenberg, *Rev. Mod. Phys.* **68**, 13 (1996).
- [5] H. v. Löhneysen, A. Rosch, M. Vojta, and P. Wölfle, *Rev. Mod. Phys.* **79**, 1015 (2007).
- [6] D. Goldhaber-Gordon, H. Shtrikman, D. Mahalu, D. Abusch-Magder, U. Meirav, and M. A. Kastner, *Nature* **391**, 156 (1998).
- [7] S. M. Cronenwett, T. H. Oosterkamp, and L. P. Kouwenhoven, *Science* **281**, 540 (1998).
- [8] J. Park, A. N. Pasupathy, J. I. Goldsmith, C. Chang, Y. Yaish, J. R. Petta, M. Rinkoski, J. P. Sethna, H. D. Abruña, P. L. McEuen, and D. C. Ralph, *Nature* **417**, 722 (2002).
- [9] V. Madhavan, W. Chen, T. Jamneala, M. Crommie, and N. Wingreen, *Science* **280**, 567 (1998).
- [10] S. Ozaki, K. Itakura, and Y. Kuramoto, *Phys. Rev. D* **94**, 074013 (2016).
- [11] D. J. Gross and F. Wilczek, *Phys. Rev. D* **8**, 3633 (1973).
- [12] H. David Politzer, *Physics Reports* **14**, 129 (1974).
- [13] P. W. Anderson, *Journal of Physics C: Solid State Physics* **3**, 2436 (1970).
- [14] K. G. Wilson, *Rev. Mod. Phys.* **47**, 773 (1975).
- [15] N. Andrei, K. Furuya, and J. H. Lowenstein, *Rev. Mod. Phys.* **55**, 331 (1983).
- [16] D. Goldhaber-Gordon, J. Göres, M. A. Kastner, H. Shtrikman, D. Mahalu, and U. Meirav, *Phys. Rev. Lett.* **81**, 5225 (1998).
- [17] C. Gonzalez-Buxton and K. Ingersent, *Phys. Rev. B* **57**, 14254 (1998).
- [18] N. Roch, S. Florens, T. A. Costi, W. Wernsdorfer, and F. Balestro, *Phys. Rev. Lett.* **103**, 197202 (2009).
- [19] J. J. Parks, A. R. Champagne, T. A. Costi, W. W. Shum, A. N. Pasupathy, E. Neuscamman, S. Flores-Torres, P. S. Cornaglia, A. A. Aligia, C. A. Balseiro, G. K.-L. Chan, H. D. Abruña, and D. C. Ralph, *Science* **328**, 1370 (2010).
- [20] Z. Iftikhar, A. Anthore, A. K. Mitchell, F. D. Parmentier, U. Gennser, A. Ouerghi, A. Cavanna, C. Mora, P. Simon, and F. Pierre, *Science* **360**, 1315 (2018).
- [21] T. A. Costi, L. Bergqvist, A. Weichselbaum, J. von Delft, T. Micklitz, A. Rosch, P. Mavropoulos, P. H. Dederichs, F. Mallet, L. Saminadayar, and C. Bäuerle, *Phys. Rev. Lett.* **102**, 056802 (2009).
- [22] A. Oguri and A. C. Hewson, *Phys. Rev. Lett.* **120**, 126802 (2018).
- [23] A. Oguri and A. C. Hewson, *Phys. Rev. B* **97**, 035435 (2018).
- [24] M. Filippone, C. P. Moca, A. Weichselbaum, J. von Delft, and C. Mora, *Phys. Rev. B* **98**, 075404 (2018).
- [25] See Supplemental Material at [URL] for derivation of Eqs. (1) and (2), expressions for $a_0(B)$, $c_T(B)$, $c(B)$, $c_V(B)$ and $s_0(B)$, $S_1(B)$, evaluations, further experimental details, fitting procedures, synthesis and characterization, results at finite temperature/thermal-bias and including Refs. [44–83].
- [26] $a_0(B)$ and $c(B)$ in (1) depend strongly on particle-hole and/or lead coupling asymmetry and are nonuniversal functions of B/T_K .
- [27] P. Nozières, *Journal of Low Temperature Physics* **17**, 31 (1974).
- [28] T. A. Costi, *Phys. Rev. Lett.* **85**, 1504 (2000).
- [29] A. Kogan, S. Amasha, D. Goldhaber-Gordon, G. Granger, M. A. Kastner, and H. Shtrikman, *Phys. Rev. Lett.* **93**, 166602 (2004).
- [30] C. H. L. Quay, J. Cumings, S. J. Gamble, R. d. Picciotto, H. Kataura, and D. Goldhaber-Gordon, *Phys. Rev. B* **76**, 245311 (2007).
- [31] A. V. Kretinin, H. Shtrikman, D. Goldhaber-Gordon, M. Hanl, A. Weichselbaum, J. von Delft, T. Costi, and D. Mahalu, *Phys. Rev. B* **84**, 245316 (2011).
- [32] T. Hata, Y. Teratani, T. Arakawa, S. Lee, M. Ferrier, R. Deblock, R. Sakano, A. Oguri, and K. Kobayashi, *Nature Communications* **12**, 3233 (2021).
- [33] A. Svilans, M. Josefsson, A. M. Burke, S. Fahlvik, C. Thelander, H. Linke, and M. Leijnse, *Phys. Rev. Lett.* **121**, 206801 (2018).
- [34] T. A. Costi, *Phys. Rev. B* **100**, 161106 (2019).
- [35] N. S. Wingreen and Y. Meir, *Phys. Rev. B* **49**, 11040 (1994).
- [36] J. E. Moore and X.-G. Wen, *Phys. Rev. Lett.* **85**, 1722 (2000).
- [37] P. Gehring, J. K. Sowa, C. Hsu, J. de Bruijkere, M. van der Star, J. J. Le Roy, L. Bogani, E. M. Gauger, and H. S. J. van der Zant, *Nature Nanotechnology* **16**, 426 (2021).
- [38] R. Van Roermund, S.-y. Shiao, and M. Lavagna, *Physical Review B* **81**, 165115 (2010).
- [39] Y. H. Zhang, S. Kahle, T. Herden, C. Stroh, M. Mayor,

- U. Schlickum, M. Ternes, P. Wahl, and K. Kern, *Nature Communications* **4**, 1 (2013).
- [40] R. Frisenda, R. Gaudenzi, C. Franco, M. Mas-Torrent, C. Rovira, J. Veciana, I. Alcon, S. T. Bromley, E. Burzurí, and H. S. J. van der Zant, *Nano Letters* **15**, 3109 (2015).
- [41] R. Gaudenzi, J. de Bruijkere, D. Reta, I. d. P. R. Moreira, C. Rovira, J. Veciana, H. S. J. van der Zant, and E. Burzurí, *ACS Nano* **11**, 5879 (2017), arXiv:1805.08126.
- [42] J. de Bruijkere, P. Gehring, M. Palacios-Corella, M. Clemente-León, E. Coronado, J. Paaske, P. Hedegård, and H. S. J. van der Zant, *Phys. Rev. Lett.* **122**, 197701 (2019).
- [43] Estimated using $B_c \approx 0.5k_B T_K^{\text{HWHM}}/g\mu_B = 0.75k_B T_K/g\mu_B$ [22, 24, 28], with $T_K^{\text{HWHM}} \approx 1.5T_K$ from Sec. SM.3.2 [25], and using T_K in Fig. 2(b).
- [44] H. Park, A. K. Lim, A. P. Alivisatos, J. Park, and P. L. McEuen, *Applied Physics Letters* **75**, 301 (1999).
- [45] K. O'Neill, E. A. Osorio, and H. S. J. Van Der Zant, *Applied Physics Letters* **90**, 10.1063/1.2716989 (2007), arXiv:0702594 [cond-mat].
- [46] P. Gehring, A. Harzheim, J. Spièce, Y. Sheng, G. Rogers, C. Evangeli, A. Mishra, B. J. Robinson, K. Porfyrakis, J. H. Warner, O. V. Kolosov, G. A. D. Briggs, and J. A. Mol, *Nano Letters* **17**, 7055 (2017).
- [47] T. A. Costi, A. C. Hewson, and V. Zlatić, *Journal of Physics: Condensed Matter* **6**, 2519 (1994), arXiv:9310032 [cond-mat].
- [48] H. R. Krishna-murthy, J. W. Wilkins, and K. G. Wilson, *Phys. Rev. B* **21**, 1003 (1980).
- [49] R. Bulla, T. A. Costi, and T. Pruschke, *Rev. Mod. Phys.* **80**, 395 (2008).
- [50] M. Lavagna, *Journal of Physics: Conference Series* **592**, 012141 (2015).
- [51] W. Hofstetter, *Phys. Rev. Lett.* **85**, 1508 (2000).
- [52] R. Peters, T. Pruschke, and F. B. Anders, *Phys. Rev. B* **74**, 245114 (2006).
- [53] A. Weichselbaum and J. von Delft, *Phys. Rev. Lett.* **99**, 076402 (2007).
- [54] R. Bulla, A. C. Hewson, and T. Pruschke, *Journal of Physics: Condensed Matter* **10**, 8365 (1998).
- [55] V. L. Campo and L. N. Oliveira, *Phys. Rev. B* **72**, 104432 (2005).
- [56] A. Rosch, T. A. Costi, J. Paaske, and P. Wölfle, *Phys. Rev. B* **68**, 014430 (2003).
- [57] L. Merker, S. Kirchner, E. Muñoz, and T. A. Costi, *Phys. Rev. B* **87**, 165132 (2013).
- [58] S. Hershfield, J. H. Davies, and J. W. Wilkins, *Phys. Rev. B* **46**, 7046 (1992).
- [59] Y. Meir and N. S. Wingreen, *Phys. Rev. Lett.* **68**, 2512 (1992).
- [60] A.-P. Jauho, N. S. Wingreen, and Y. Meir, *Phys. Rev. B* **50**, 5528 (1994).
- [61] C. Mora, C. P. Moca, J. von Delft, and G. Zaránd, *Phys. Rev. B* **92**, 075120 (2015).
- [62] A. A. Aligia, P. Roura-Bas, and S. Florens, *Phys. Rev. B* **92**, 035404 (2015).
- [63] S. Amasha, I. J. Gelfand, M. A. Kastner, and A. Kogan, *Phys. Rev. B* **72**, 045308 (2005).
- [64] A. A. Houck, J. Labaziewicz, E. K. Chan, J. A. Folk, and I. L. Chuang, *Nano Letters* **5**, 1685 (2005), pMID: 16159205, <https://doi.org/10.1021/nl050799i>.
- [65] T.-M. Liu, B. Hemingway, A. Kogan, S. Herbert, and M. Melloch, *Phys. Rev. Lett.* **103**, 026803 (2009).
- [66] M. Yoshida, A. C. Seridonio, and L. N. Oliveira, *Phys. Rev. B* **80**, 235317 (2009).
- [67] T. A. Costi and V. Zlatić, *Phys. Rev. B* **81**, 235127 (2010).
- [68] C. Lacroix, *Journal of Physics F: Metal Physics* **11**, 2389 (1981).
- [69] U. Eckern and K. I. Wysokiński, *New Journal of Physics* **22**, 013045 (2020).
- [70] B. E., (2016), max-Planck Institute for Chemical Energy Conservation, Mülheim, available from the author by mail on eckhard.bill@cec.mpg.de.
- [71] E. Pyurbeeva, C. Hsu, D. Vogel, C. Wegeberg, M. Mayor, H. van der Zant, J. A. Mol, and P. Gehring, *Nano Letters* **21**, 9715 (2021), arXiv:2109.06741.
- [72] J. L. Turnbull, B. R. Benlian, R. P. Golden, and E. W. Miller, *Journal of the American Chemical Society* **143**, 6194 (2021), publisher: American Chemical Society.
- [73] C. Hirel, K. E. Vostrikova, J. Pécaut, V. I. Ovcharenko, and P. Rey, *Chemistry – A European Journal* **7**, 2007 (2001).
- [74] W. K. Wilmarth and N. Schwartz, *Journal of the American Chemical Society* **77**, 4543 (1955), publisher: American Chemical Society.
- [75] G. V. Romanenko, S. V. Fokin, S. E. Tolstikov, G. A. Letyagin, A. S. Bogomyakov, and V. I. Ovcharenko, *Journal of Structural Chemistry* **61**, 906 (2020).
- [76] D. Wang, Y. Ma, B. Wolf, A. I. Kokorin, and M. Baumgarten, *The Journal of Physical Chemistry A* **122**, 574 (2018), publisher: American Chemical Society.
- [77] S. I. Zhivetyeva, I. A. Zayakin, I. Y. Bagryanskaya, E. V. Zaytseva, E. G. Bagryanskaya, and E. V. Tretyakov, *Tetrahedron* **74**, 3924 (2018).
- [78] T. J. Stone, T. Buckman, P. L. Nordio, and H. M. McConnell, *Proceedings of the National Academy of Sciences* **54**, 1010 (1965), publisher: National Academy of Sciences Section: Research Article.
- [79] V. Chechik, H. J. Wellsted, A. Korte, B. C. Gilbert, H. Caldararu, P. Ionita, and A. Caragheorgheopol, *Faraday Discussions* **125**, 279 (2004), publisher: The Royal Society of Chemistry.
- [80] K. Tsutsumi, Y. Teratani, R. Sakano, and A. Oguri, *Phys. Rev. B* **104**, 235147 (2021).
- [81] E. Sela and J. Malecki, *Phys. Rev. B* **80**, 233103 (2009).
- [82] A. A. Aligia, *Journal of Physics: Condensed Matter* **24**, 015306 (2012).
- [83] M. A. Sierra, R. López, and D. Sánchez, *Phys. Rev. B* **96**, 085416 (2017).

Supplemental Material for Magnetic Field Universality of the Kondo Effect Revealed by Thermocurrent Spectroscopy

Chunwei Hsu,¹ Theo A. Costi,^{2,3} David Vogel,⁴ Christina Wegeberg,⁴
Marcel Mayor,^{4,5,6} Herre van der Zant,¹ and Pascal Gehring^{1,7,*}

¹*Kavli Institute of Nanoscience, Delft University of Technology,
Lorentzweg 1, Delft 2628 CJ, The Netherlands*

²*Peter Grünberg Institut, Forschungszentrum Jülich, 52425 Jülich, Germany*

³*Institute for Advanced Simulation, Forschungszentrum Jülich, 52425 Jülich, Germany*

⁴*Department of Chemistry, University of Basel,
St. Johannis-Ring 19, 4056 Basel, Switzerland*

⁵*Institute for Nanotechnology (INT), Karlsruhe Institute of Technology (KIT),
P.O. Box 3640, 76021 Karlsruhe, Germany*

⁶*Lehn Institute of Functional Materials (LIFM), School of Chemistry,
Sun Yat-Sen University (SYSU), 510275 Guangzhou, China*

⁷*IMCN/NAPS, Université Catholique de Louvain (UCLouvain), 1348 Louvain-la-Neuve, Belgium*

(Dated: April 12, 2022)

CONTENTS

SM.1. Methods	3
SM.1.1. Device fabrication.	3
SM.1.2. Lock-in modulation technique.	3
SM.1.3. Extraction of the Kondo temperature.	4
SM.1.4. Fitting $s_1^{\text{exp.}}(B)$ to the universal curve $s_1(B)/s_1(0)$.	4
SM.2. Additional experimental results	5
SM.2.1. Experimental data on molecular quantum dot QD2	5

* Email: pascal.gehring@uclouvain.be

	2
SM.2.2. Proportionality between $-d^2I/dV_{sd}^2$ and I_{th}	6
SM.2.3. Gaussian filter for electronic cross-talk	6
SM.2.4. Temperature dependence of QD1	8
SM.2.5. Thermal bias dependent measurement of QD1	10
SM.2.6. Temperature calibration by Kondo peak	12
SM.2.7. Stability diagram of the QD1	14
SM.3. Nonlinear thermocurrent of Kondo-correlated quantum dots in a magnetic field:	
Theory	15
SM.3.1. Model	15
SM.3.2. Kondo scales	16
SM.3.3. Nonlinear transport quantities	18
SM.3.4. Nonlinear thermocurrent for $\Delta T \ll T$ and asymmetric couplings	19
SM.3.5. Nonlinear thermocurrent and dI/dV : higher-order Fermi-liquid theory and NRG calculations	21
SM.3.5.1. Splitting of the Kondo resonance in dI/dV and A	23
SM.3.5.2. Experimental estimates of the splitting field B_c	27
SM.3.5.3. Thermocurrent $I_{th}(V)$ versus V in the Fermi-liquid regime	28
SM.3.5.4. Universal scaling functions for $s_1(B)$ and $c_V(B)$	31
SM.3.5.5. Zero-bias thermocurrent and zero-bias thermocurrent slope	33
SM.3.5.6. Temperature and thermal bias effects	34
SM.3.6. Equation of motion method for nonlinear thermoelectric transport	34
SM.3.6.1. Equation of motion method and numerical calculations	35
SM.3.6.2. Model parameters and ranges for V, B, T and ΔT	38
SM.3.6.3. Magnetic field dependence	39
SM.3.6.4. Thermal bias dependence	39
SM.3.6.5. Temperature dependence	44
SM.3.6.6. Proportionality between I_{th} and d^2I/dV^2 at $\Delta T \ll T \ll T_K$	45
SM.4. Synthesis & characterization of the organic radical	47
SM.4.1. Synthesis	48
SM.4.2. Electron paramagnetic resonance spectroscopic analysis of the nitronyl nitroxide Radical (NNR) 8	50

SM.1. METHODS

SM.1.1. Device fabrication.

The thermoelectric device is fabricated by standard electron-beam lithography with a double-layer PMMA 495K/950K resist and electron-beam evaporation deposition technique. First, the local back gate (dark purple pattern in Fig. 1d) with Ti+Pd thickness of 1+7 nm is created on a SiO₂/Si wafer with an oxide thickness of 817 nm. The heaters (light blue pattern) are fabricated with Ti+Pd at a thickness of 3+27 nm subsequently. Afterwards, a insulating layer of Al₂O₃ of 10 nm is deposited with an atomic layer deposition technique at 300 °C. The Au bridge (golden pattern) is then made with a thickness of 12 nm without an adhesive layer. Finally the contact electrodes (orange pattern) of Ti+Au thickness of 5+65 nm are made to connect the Au bridge made in the previous step.

After the fabrication steps, the device is wire-bonded, mounted onto a variable temperature insert and pumped down. A high current with a feedback control is used to initiate the electromigration of the Au bridge in vacuum [1]. A nm-sized gap is formed by electromigration and self-breaking [2]. After the successful electromigration, the nanogap was then immersed in a molecular solution of 1 mM dissolved in dichloromethane. The sample was immediately pumped and cooled down to 2.0 K to prevent further opening of the electromigrated nanogap and potential degradation of the radical molecule.

SM.1.2. Lock-in modulation technique.

After device formation and cool down, the electrical and thermoelectric measurements are carried out. In order to measure the electrical and thermoelectric signals at the same time, we employ a lock-in technique [3], where the AC thermal bias $\Delta\tilde{T}$ and electrical bias \tilde{V}_{sd} were applied at two different frequencies. The differential conductance (dI/dV_{sd}) of the quantum dot was directly obtained with a lock-in amplifier. In a typical experiment $\tilde{V}_{sd} = 100\mu\text{V}$ at $\omega_1 = 13$ Hz is used. A thermal bias at a frequency $\omega_2 = 3$ Hz is applied by

the microheater and the resulting thermocurrent (I_{th}) through the quantum dot is measured at the second harmonic $2\omega_2$ with respect to the excitation [4].

SM.1.3. Extraction of the Kondo temperature.

The temperature dependence of the zero-bias peak for a spin-1/2 Kondo effect, calculated within NRG [5], is well described by the empirical formula [6].

$$G(T) = G_l \left(\frac{T^2}{T_K^2} (2^{1/s} - 1) + 1 \right)^{-s} + G_c, \quad (\text{S1})$$

where $G_l = \frac{2e^2}{h} \frac{4\Gamma_s\Gamma_d}{(\Gamma_s+\Gamma_d)^2}$ is the maximum conductance peak reached at $T \ll T_K$, $s = 0.22$ for a spin-1/2 Kondo effect, G_c is the background conductance which is additional to the Kondo resonance due to a direct tunneling/parallel channel in the quantum dot. Equation (S1) defines the Kondo temperature T_K as $G(T = T_K) - G_c = (G(T = 0) - G_c)/2$. The fitting of Eq. (S1) is shown Fig. 2b as a function of temperature after subtracting the background conductance, resulting in $T_K = 12.8$ K.

SM.1.4. Fitting $s_1^{\text{exp.}}(B)$ to the universal curve $s_1(B)/s_1(0)$.

In the Kondo regime of a spin-1/2 quantum dot with asymmetric lead couplings $\Gamma_d \gg \Gamma_s$, the universal curve for $s_1(B)/s_1(0) = f_1(b)$ with $b = g\mu_B B/k_B T_K$ can be calculated within NRG for all b (SM.3.5.3). An approximate interpolation formula for this function, valid for a large range of b from $b \ll 1$ to $b \gg 1$, is given by (SM.3.5.4)

$$f_1(b) = \frac{(1 - \alpha_0 b^2)}{(1 + \beta_0 b^2)^z}, \quad (\text{S2})$$

where $\alpha_0 \approx 1.77$, $\beta_0 \approx 1.12$ and $z \approx 2.6$. We used Eq. (S2) to carry out a least-squares fit of $r \times s_1^{\text{exp.}}(B)$ to $f_1(b)$, yielding $r = 2.18 \times 10^6 \text{ mVnA}^{-1}$.

SM.2. ADDITIONAL EXPERIMENTAL RESULTS

SM.2.1. Experimental data on molecular quantum dot QD2

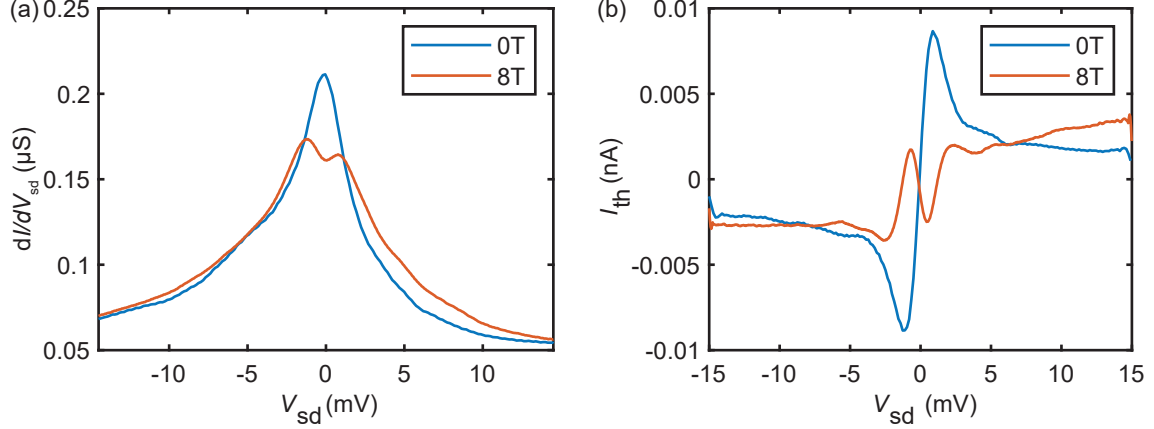


FIG. S1. (a) Measured dI/dV_{sd} of QD2 at magnetic fields of 0 and 8 T. (b) Measured I_{th} of QD2 at magnetic fields of 0 and 8 T.

An additional set of data on a different molecular quantum dot device, QD2, is presented in Fig. S1. The experimental dI/dV_{sd} and I_{th} of QD2 are shown in Fig. S1a,b respectively. Worth-noting, the coupling between the molecule and the electrodes is smaller than that of the device shown in the main text (we denote the quantum dot in the main text by QD1 in the following). This is seen readily by the smaller HWHM of the zero-bias peak and the smaller base-line dI/dV_{sd} . Due to this weaker coupling, meaning a lower T_K and B_c , a splitting of dI/dV_{sd} at zero bias is observed at $B = 8$ T, different from the case of QD1. The I_{th} of QD2 presented in Fig. S1b shows the same trend as in Fig. 3b. At $B = 0$ T, from $V_{sd} < 0$ to $V_{sd} > 0$, I_{th} first goes to a large negative value, crossing the origin and then to a large positive value, in a S-like shape. At $B = 8$ T, a "kink" appears as the slope of I_{th} changes its sign at $V_{sd} = 0$, similar to the case in Fig. 3b of QD1. This additional set of measurement provides an example where the splitting of dI/dV_{sd} is comparable to the kink of I_{th} , consistent with the calculations shown in the main text. However, further magnetic and temperature dependence of QD2 was unable to be obtained as the sample was damaged in a measurement with high heater current.

SM.2.2. Proportionality between $-d^2I/dV_{sd}^2$ and I_{th}

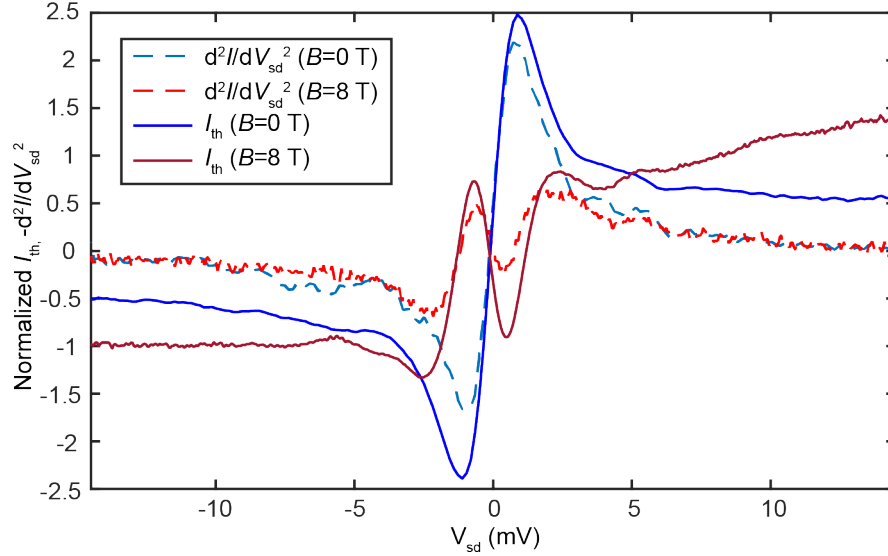


FIG. S2. Normalized $-d^2I/dV_{sd}^2$ and I_{th} of QD2.

In the weaker coupling case of QD2, an interesting feature is observed by taking the derivative of dI/dV_{sd} in Fig S1. Here, by plotting the normalized value of $-d^2I/dV_{sd}^2$ on top of I_{th} , a proportionality between the two quantities is observed as shown in Fig. S2. This experimental observation is further discussed theoretically in the later section of SM.3.6.6.

SM.2.3. Gaussian filter for electronic cross-talk

In the simultaneous stimulation of dI/dV_{sd} and I_{th} with lock-in amplifiers, oscillations in the measured signals are observed in the measurements as a result of electronics cross-talk. Therefore, a Gaussian filter is applied to the high frequency oscillations in the measurements to restore the measurement signals. The implementation of Gaussian filter is basically weighted moving average function and can be found in the *smoothdata* function in the proprietary software Matlab with version of 2017b and newer.

Figure S3a,b show an example of unfiltered data of Fig. 2 of QD1. A periodic interference in both dI/dV_{sd} and I_{th} can be observed as a result of lock-in cross-talk. With the Gaussian filter described above, we obtain the restored signal in Fig. 2,3 in the main text. The error bars are estimated from the moving standard deviation on the raw data, using *movstd* in

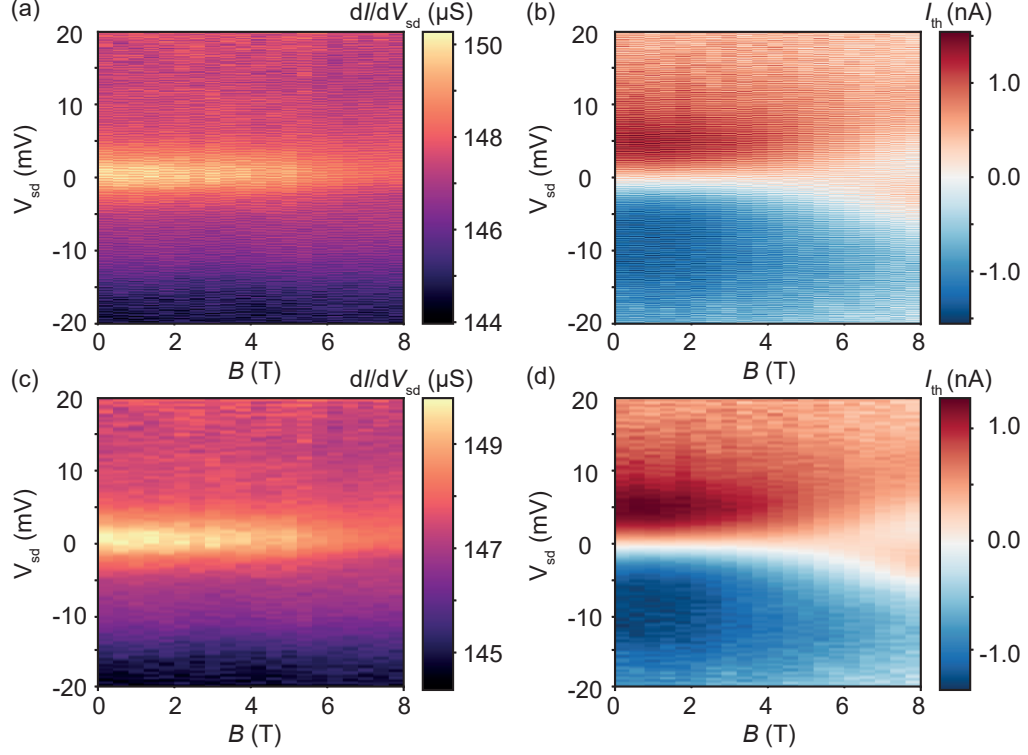


FIG. S3. (a)-(b) Unfiltered data of the electronic/thermoelectric measurement of the quantum dot shown in Fig. 2,3 (QD1). (c)-(d) Fast-Fourier-Transform (FFT) Filtering of data in (a)-(b). The data with electronic cross-talk is rectified with a FFT filter, where frequency components smaller than $1/3$ of maximum frequency in the Fourier domain are kept.

Matlab. This gives error bars around $0.5 \mu\text{S}$ for Fig. 2a,c and d, which are not plotted in the main text figure for data visibility. To better demonstrate the effect of Gaussian filter applied in the main text, we also show another commonly used Fast-Fourier transform filter as a comparison in Fig. S3c,d. In this case we rectify the data by cutting off Fourier components with frequency that are larger than $1/3$ of maximum frequency in the frequency domain. Essentially, both the Gaussian and FFT filters have a similar effect on the data and filter out the periodic interference. By comparing the two methods, it is clear that the underlying features can be restored as long as the interference signal is periodic.

SM.2.4. Temperature dependence of QD1

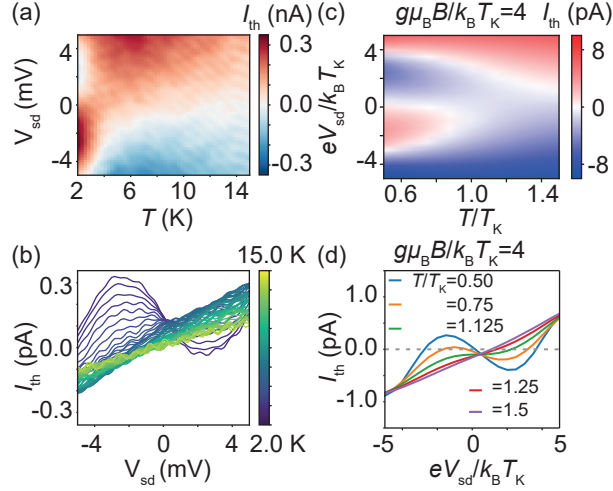


FIG. S4. (a)-(b) Temperature dependent thermocurrent measurement of QD1 at a magnetic field 8 T above B_{th} . (c)-(d) Calculated temperature dependence of thermocurrent at a magnetic field $B > B_{th}$ using the approximate nonequilibrium equation of motion method of Sec. SM.3.6.

In the Letter, we presented measurements of the magnetic field dependence of the thermocurrent in the low temperature strong coupling regime ($T \ll T_K$). We showed that the zero-bias thermocurrent slope changes sign from positive to negative (i.e., a kink develops at zero-bias) upon increasing the magnetic field above B_{th} with $B_{th} = 6.6$ T. Here, we investigate how this kink in I_{th} , present for $B > B_{th}$ and $T \ll T_K$, behaves with increasing temperature. Figs. S4(a) and (b) show results for a specific field $B = 8$ T ($> B_{th}$). One sees, that the kink vanishes above a certain temperature. For the case shown ($B=8$ T), this temperature is approximately 5 K. The temperature above which the kink in I_{th} vanishes is not universal (e.g., it will depend on the value of $B > B_{th}$) and is not simply related to T_K . Thus one cannot extract T_K from the vanishing of the kink with increasing temperature. Calculations at finite temperatures (comparable to T_K) lie outside the regime of validity of the asymptotically exact Fermi-liquid theory used to explain the B -dependence of the low temperature thermocurrent in the strong coupling regime ($\Delta T \ll T \ll T_K$) in the Letter. In order to explain the observations, we therefore resort to an approximate nonequilibrium equation of motion approach (Sec. SM.3.6). The results, shown in Figs. S4(c) and (d) for $B > B_{th}$, capture the observed experimental trends, including the vanishing of the kink

in the thermocurrent above a certain nonuniversal temperature ($T \approx 1.125T_K$ for the case shown).

SM.2.5. Thermal bias dependent measurement of QD1

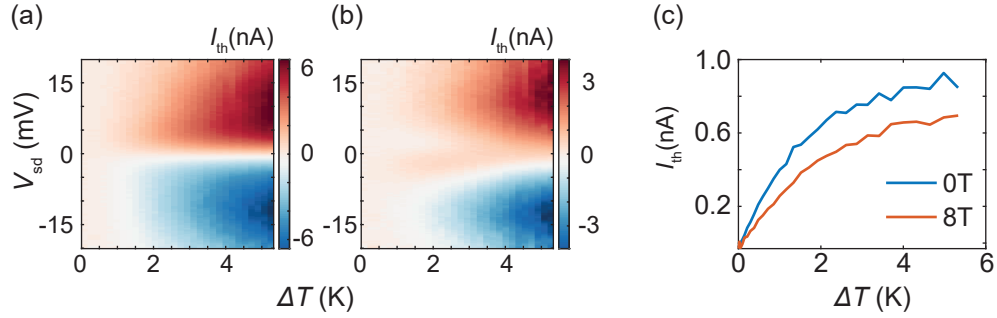


FIG. S5. (a)-(b), Thermal bias dependence of I_{th} at $B = 0$ T and $B = 8$ T. (c), Zero-bias I_{th} as a function of thermal bias, ΔT .

To further investigate the nonlinear effect caused by the thermal gradient (ΔT), we study the thermocurrent response of the device as a function of thermal bias. As shown in Fig. S5(a), at zero magnetic field and finite bias, I_{th} increases as ΔT rises. At first sight, this increase can be understood as a result of the change in thermal bias, which can be seen directly from the definition, $I_{th} = -L\Delta T$, in the linear response regime. Nonetheless, as we consider I_{th} as a function of ΔT at a fixed bias voltage, a clear non-linear relation is observed (see Fig. S5(c) for the case at zero-bias), indicating the non-linear regime.

The Kondo feature, in the form of thermocurrent, changes as ΔT increases in this non-linear regime. Figure S5(b) shows I_{th} as a function of ΔT at 8 T, where the same kink presented in Fig. 3a,b is observed at low ΔT . This inversion is suppressed when ΔT increases above a value of about 2 K. There are two contributions to this disappearance of the inversion in I_{th} at zero-bias. First, this can come from the global heating of the sample which raises the base temperature of the junction. By comparing the Kondo-peak height at different ΔT and T (see SM.2.6), we can roughly estimate that for a $\Delta T \approx 5$ K, the junction temperature is increased to $T \approx 5$ K rather than 2 K. This is consistent with the observation in Fig. S4(a), where thermocurrent inversion around zero-bias disappears also around 5 K. Another possible contribution for this absence of inversion at 8 T with $\Delta T > 2$ K can also originate from the population of off-resonant levels by the thermal bias. This results the mixing for the Zeeman-split levels and smears out the inversion observed in I_{th} .

The above observations shows that our thermal bias dependent measurement successfully probes the non-linear thermoelectric regime, in combination with the Kondo effect. Partic-

ularly, the increasing of zero-bias I_{th} with a split spectral function upon the increase of ΔT , demonstrates the breaking of particle-hole symmetry, or a large shift in the off-resonance levels upon the splitting of the Kondo spectral function at ΔT . Such non-linear regime is addressed theoretically in Sec. SM.3.

SM.2.6. Temperature calibration by Kondo peak

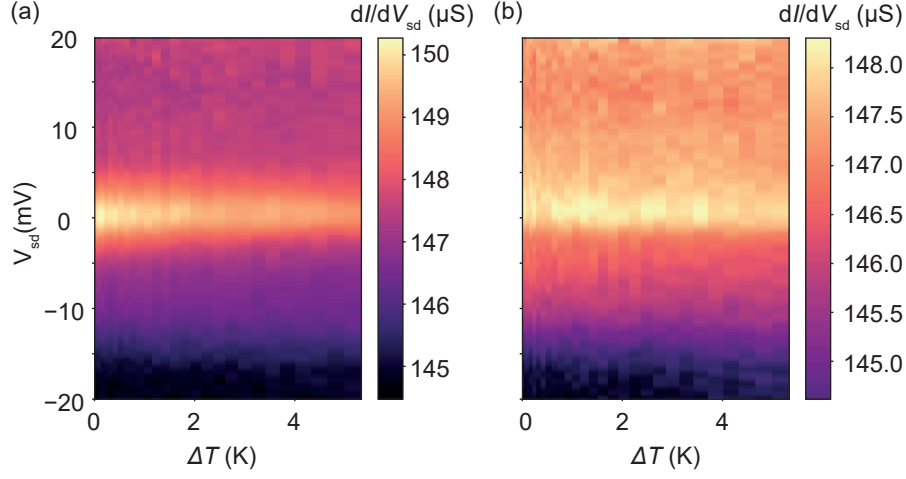


FIG. S6. (a)-(b) Differential conductance of QD1 as a function of thermal bias ΔT at (a) $B=0$ T, and, (b) $B=8$ T.

The thermal bias generated by the heater can also heat up the base temperature at the molecular quantum dot. To get an estimate of the local base temperature at this position, we use the Kondo peak amplitude at $B = 0$ T as a conversion from thermal bias ΔT to the local base temperature T . The Kondo peak amplitudes at different ΔT and T are extracted from Fig. S6(a) and Fig. S4(a) respectively. In the case of Fig. S6, the global sample space was kept at 2 K while the local thermal bias was swept to 5.32 K; in the case of Fig. S4, the local thermal bias was kept at 0.59 K while the global sample space temperature is swept from 2 to 15 K. We first plot ΔT as a function of peak amplitude, which reaches 0 at peak amplitude above 3.6 μS , indicating negligible heating at the molecular quantum dot (blue curve). We then plot T as a function of peak amplitude (red curve). Therefore, for a fixed ΔT we can find the corresponding peak amplitude, which also corresponds to a fixed T (Fig. S7). For example, for $\Delta T = 3$ K, we find a peak amplitude close to 2.8 μS which translates to a base temperature of about 4.5 K. Note that the red curve is offset vertically by 0.8 K such that the global sample temperature $T = 2$ K corresponds to an amplitude of 3.6 μS , where only negligible thermal bias is generated.

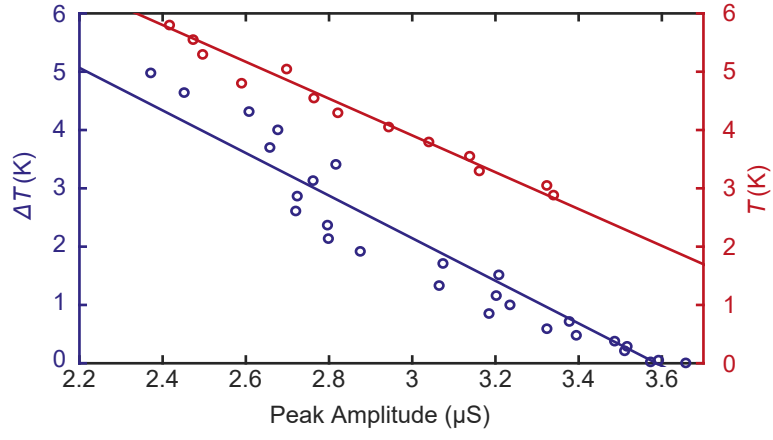


FIG. S7. Estimated base temperature T (K), at different Kondo peak amplitudes and ΔT .

SM.2.7. Stability diagram of the QD1

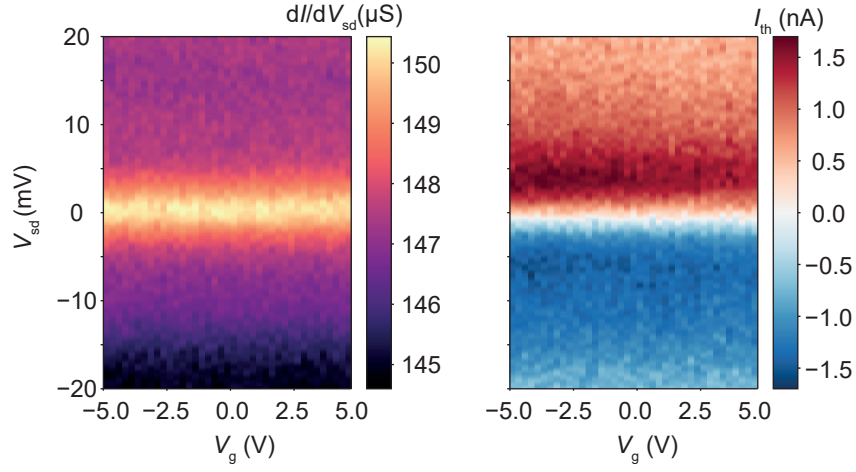


FIG. S8. Stability diagram of QD1.

The experimental results of the molecular quantum dot shown in the main text are measured without a gate. This is due to the small gate coupling as can be observed in Fig. S8. The high differential conductance ($2 G_0$) here also indicates that the coupling between the source/drain leads to the dot is high as compared to the coupling to the gate.

SM.3. NONLINEAR THERMOCURRENT OF KONDO-CORRELATED QUANTUM DOTS IN A MAGNETIC FIELD: THEORY

This section provides a theory of the nonlinear thermocurrent $I_{\text{th}}(V, T, B, \Delta T)$ of Kondo-correlated quantum dots in the presence of a magnetic field. For $\Delta T \ll T \ll T_K$ and $V \ll T_K$, we use an asymptotically exact higher-order Fermi-liquid theory [7, 8] combined with numerical renormalization group (NRG) calculations [9, 10] to evaluate I_{th} to lowest order in ΔT and V , while for $\Delta T, T$ and V comparable to, or larger than T_K we use an approximate nonequilibrium Green function equation of motion method [11, 12] to map out the trends in the voltage, temperature and thermal bias dependence of the thermocurrent at different magnetic fields (Sec. SM.3.6). Within the former, we show that the zero-bias slope of the thermocurrent $s_1(B) = (\partial I_{\text{th}}(V)/\partial V)_{V=0}$ changes sign at a certain field B_{th} as observed in the experiment. Moreover, we show that B_{th} coincides essentially exactly with the field B_c at which the Kondo resonance in the differential conductance splits (Sec. SM.3.5.3) and also that $s_1(B)$ is a universal function of B/T_K (Sec. SM.3.5.4). Significant deviations from these results only arise for weak correlations or outside the Kondo regime (e.g. on approaching the mixed valence regime). All NRG calculations used the full density matrix approach to spectral functions [13–15] and the self-energy method [16] and the Campo discretization scheme [17] with discretization parameter $\Lambda = 4$ and z-averaging with $N_z = 4$.

SM.3.1. Model

Our starting point is the two-lead single-level Anderson impurity model,

$$H = H_{\text{dot}} + H_{\text{leads}} + H_{\text{tunneling}}. \quad (\text{S3})$$

The first term, $H_{\text{dot}} = \sum_{\sigma} \varepsilon_{0\sigma} n_{0\sigma} + U n_{0\uparrow} n_{0\downarrow}$, describes the dot Hamiltonian, where $\varepsilon_{0\sigma}$ is the level energy with spin σ , $n_{0\sigma} = d_{0\sigma}^\dagger d_{0\sigma}$ is the occupation number for spin $\sigma = \uparrow, \downarrow$ electrons on the dot, and $U = 2E_C$ is the local Coulomb repulsion on the dot with $E_C = e^2/2C$ the charging energy of the dot with capacitance C and e is the elementary charge. The dot level energy $\varepsilon_{0\sigma} = \varepsilon_0 - g\mu_B B\sigma/2$ includes the Zeeman shift $\pm g\mu_B B/2$ of the level ε_0 where g is the g-factor, μ_B is the Bohr magneton and B is the local magnetic field. We shall work at a fixed (dimensionless) gate voltage $V_g \equiv (\varepsilon_0 + U/2)/\Gamma$ in the Kondo regime (as in the experiments) with $V_g = 0$ corresponding to the particle-hole symmetric (mid-valley) point.

The second term, $H_{\text{leads}} = \sum_{k\alpha\sigma} \epsilon_{k\alpha} c_{k\alpha\sigma}^\dagger c_{k\alpha\sigma}$, describes the leads, where $\alpha = L, R$ labels the left (source) and right (drain) leads, and $\epsilon_{k\alpha\sigma} = \epsilon_k - \mu_\alpha$ is the kinetic energy of the lead electrons, each measured relative to their respective chemical potential $\mu_{\alpha=L,R}$. The bias voltage V across the dot is defined in terms of the difference of chemical potentials between left and right leads via $-eV = \mu_L - \mu_R$. Furthermore, we assume that the voltage drops symmetrically across the leads, i.e., $\mu_L = -eV/2$ and $\mu_R = +eV/2$. In the notation of Ref. 7, where the voltage drop across the leads is written as $\mu_L = \alpha_L eV$ and $\mu_R = -\alpha_R eV$, our choice corresponds to $\alpha_L = \alpha_R = -1/2$ with $\alpha_L + \alpha_R = -1$. The Fermi distributions of the leads are given by $f_\alpha^{T_\alpha}(\omega) = f((\omega - \mu_\alpha)/k_B T_\alpha)$ where $f(x) = 1/(1 + e^x)$ is the Fermi function and $T_{\alpha=L,R}$ are the temperatures of the left and right lead electrons. As in the experiment, we take the left lead to be the hot electrode with temperature $T_L = T_R + \Delta T$ where ΔT is the finite temperature difference across the dot. In the experiment, the thermal temperature difference is determined by the heater power used to heat the left electrode above the base temperature T , which is also the temperature of the right electrode, i.e., $T_R = T$. Finally, the last term in the Hamiltonian, $H_{\text{tunneling}} = \sum_{k\alpha\sigma} t_\alpha (c_{k\alpha\sigma}^\dagger d_\sigma + d_\sigma^\dagger c_{k\alpha\sigma})$, describes the tunneling of electrons from the leads onto and off the dot with tunneling amplitudes t_α . The corresponding tunneling rates are given by $\Gamma_\alpha = \pi N_F t_\alpha^2$, where $N_F = 1/(2D)$ is the energy independent lead electron density of states and $D = 1$ is the half bandwidth of the leads. The total tunneling rate on and off the dot is denoted by $\Gamma = \Gamma_L + \Gamma_R$ and the asymmetry parameter of the lead couplings is defined by $\lambda = \Gamma_L/\Gamma_R$. Note that Γ corresponds to the half-width of a Coulomb Blockade peak, the usual notation for theoretical work on the Anderson model [18]. In the literature on quantum dots, the full width $\tilde{\Gamma} = 2\Gamma$ is often used.

SM.3.2. Kondo scales

For strong correlations $U/\Gamma \gg 1$ and local level position $\varepsilon_0/\Gamma \ll -1$, and $(\varepsilon_0 + U)/\Gamma \gg +1$ the quantum dot level is approximately singly occupied with $n_0 = \sum_\sigma \langle n_{0\sigma} \rangle \approx 1$ and has a spin 1/2, resulting in the well known Kondo effect[18], in which physical properties undergo a crossover from those of a weakly coupled system at $g\mu_B B, |e|V, k_B T \gg k_B T_K$ to those of a strongly coupled system at $g\mu_B B, |e|V, k_B T \ll k_B T_K$, where the low energy crossover scale $k_B T_K$ is termed the Kondo scale, and T_K is the Kondo temperature. In applying theory

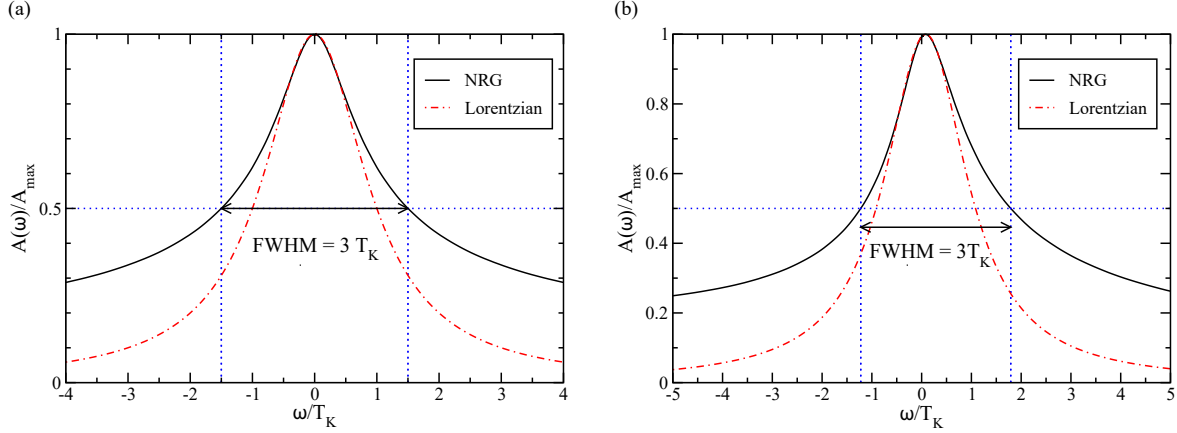


FIG. S9. Numerical renormalization group calculation of the low energy Kondo resonance in the $T = V = B = 0$ normalized spectral function $A(\omega)/A_{\max}$ of the Anderson impurity model for $U = 8\Gamma$. A_{\max} is the maximum value of $A(\omega)$. The spectral function is plotted versus ω/T_K , where T_K is the Kondo scale from the susceptibility in Eq. (S22). (a) Symmetric case ($\varepsilon_0 = -U/2 = -4\Gamma$). (b) asymmetric case ($\varepsilon_0 = -3\Gamma$). In both cases, the FWHM of the Kondo resonance is very close to $3T_K$, showing that $T_K^{\text{HWHM}} \approx 1.5T_K$ [19]. Note also, that a noninteracting resonant level of width T_K , described by a Lorentzian (dashed-dotted lines), while approximately capturing the behavior of the Kondo resonance at $\omega \ll T_K$, inevitably fails to describe the correct lineshape of the Kondo resonance at higher energies. For $\omega \gg T_K$, the latter is better described by logarithmic tails [20].

predictions that use a certain definition of T_K to interpret an experiment that uses another definition of T_K , one needs to know the relation between the different Kondo scales. We therefore briefly outline the the Kondo scales relevant to the present study and how they are related.

The first, T_K^G , is extracted from temperature dependence of the universal Kondo conductance curve, $G_K(T)$, via $G(T_K^G) = G(0)/2$. The second is defined below in Eq. (S22) via the $T = 0$ spin susceptibility, and will be denoted as T_K . It is the natural scale to use for the higher-order Fermi-liquid theory calculations below. Since T_K and T_K^G have been shown to lie within a few % of each other in the Kondo regime [21], we shall equate them $T_K \approx T_K^G$. Another commonly used Kondo scale is Haldane's expression from perturbative scaling on the asymmetric Anderson impurity model, $T_K^H = \sqrt{U\Gamma/2}e^{\pi\varepsilon_0(\varepsilon_0+U)/2\Gamma U}$ [18]. This shows explicitly the (approximate) dependence of the Kondo scale on the model parameters

Γ, ε_0 and U in the Kondo limit and for $U \gg \Gamma$. We shall not use it in this paper. We simply mention that it is of order T_K (e.g., for typical parameters $\varepsilon_0 = -6\Gamma$ and $U = 8\Gamma$ in the asymmetric Kondo regime we find $T_K^H \approx 0.84T_K$). Finally, since the splitting of the Kondo resonance in a magnetic field was first discussed in terms of the scale T_K^{HWHM} , defined as the half-width at half-maximum of the $T = 0$ Kondo resonance [22], we make reference to this scale also. In particular, using the relation $T_K^{\text{HWHM}} \approx 1.5T_K$ [see Fig. S9] allows one to express the original estimate of the splitting field $g\mu_B B_c \approx 0.5k_B T_K^{\text{HWHM}}$ [22] in terms of recent estimates of this within higher-order Fermi-liquid theory which use instead T_K . Thus, in terms of T_K , we have $g\mu_B B_c \approx 0.75k_B T_K$, which is indeed the result found in higher-order Fermi-liquid theory [8, 23]. The slower decay of the Kondo resonance away from the Fermi level, as compared to a Lorentzian for a non-interacting level, accounts for the 50% larger linewidth of the former. This is also expected due to the onset of logarithmic tails at higher energies $|\omega| \gg T_K$ [20].

In a few places below, we shall, for the sake of brevity, omit physical units in expressions such as B/T_K or V/T_K . In such cases, these should be understood as meaning $g\mu_B B/k_B T_K$ and $eV/k_B T_K$, respectively.

SM.3.3. Nonlinear transport quantities

The electrical current $I = I(V, T, B, \Delta T)$ is defined as the current in the left lead, i.e., $I \equiv I_L = -e\langle \dot{N}_L \rangle$, where $N_L = \sum_{k\sigma} \langle c_{kL\sigma}^\dagger c_{kL\sigma} \rangle$ is the number of electrons in the left lead. Likewise, the current in the right lead is defined by $I_R = -e\langle \dot{N}_R \rangle$, where $N_R = \sum_{k\sigma} \langle c_{kR\sigma}^\dagger c_{kR\sigma} \rangle$ is the number of electrons in the right lead. By current conservation, we have that $I_L + I_R = 0$, or $I_R = -I_L = -I$. An explicit expression for the current can be derived in terms of the lesser, retarded and advanced Green functions of the dot [24, 25]. However, since we use proportionate couplings $\Gamma_L = \lambda\Gamma_R$, the dependence of the current on the lesser Green function can be eliminated [26], resulting in an expression for the current in terms of the difference of retarded and advanced Green functions, i.e., in terms of solely the nonequilibrium spectral function $A_\sigma(\omega, V, T, B, \Delta T)$ [27] of the dot [24–26],

$$I(V, T, B, \Delta T) = -\frac{2e}{\hbar} \sum_{\sigma} \int d\omega \frac{\Gamma_L \Gamma_R}{\Gamma} [f_L^{T+\Delta T}(\omega) - f_R^T(\omega)] A_\sigma(\omega, V, T, B, \Delta T), \quad (\text{S4})$$

$$= \gamma \int d\omega [f_L^{T+\Delta T}(\omega) - f_R^T(\omega)] A(\omega, V, T, B, \Delta T). \quad (\text{S5})$$

In the above, $\gamma = -2e\Gamma_L\Gamma_R/(\hbar\Gamma)$ and $A(\omega, V, T, B, \Delta T) = \sum_{\sigma} A_{\sigma}(\omega, V, T, B, \Delta T)$ is the total spectral function of the dot. The thermocurrent, I_{th} , is then defined as the difference of the electrical currents at finite and zero thermal bias ΔT ,

$$I_{\text{th}}(V, T, B, \Delta T) = I(V, T, B, \Delta T) - I(V, T, B, \Delta T = 0). \quad (\text{S6})$$

The differential conductance

$$G(V, T, B) = \frac{dI}{dV}, \quad (\text{S7})$$

is obtained from the current at zero thermal bias $\Delta T = 0$. From Eq. (S5), the linear conductance $G_l = G(V = 0, T, B)$ at $T = B = 0$ is given by

$$G_l = \gamma e A(0, 0, 0, 0) = \frac{2e^2}{h} \frac{4\Gamma_L\Gamma_R}{\Gamma^2} \sin^2(\pi n_0/2) \leq G_{\text{max}}, \quad (\text{S8})$$

where $G_{\text{max}} = G_0 4\Gamma_L\Gamma_R/\Gamma^2$, $G_0 = 2e^2/h$ is the conductance quantum and we used the Fermi-liquid result for the spectral function $A(0, 0, 0, 0) = \frac{2}{\pi\Gamma} \sin^2(\pi n_0/2) \leq \frac{2}{\pi\Gamma}$ (with equality at mid-valley when $n_0 = 1$). We shall use G_{max} as a normalization in showing dI/dV results in Secs. SM.3.6.3-SM.3.6.6. Note that while $G_{\text{max}} = G_0$ for symmetric coupling to the leads, for the molecular quantum dot in the experiment, the lead couplings are highly asymmetric $\Gamma_L = \lambda\Gamma_R \ll \Gamma_R$ and $G_{\text{max}} \ll G_0$.

SM.3.4. Nonlinear thermocurrent for $\Delta T \ll T$ and asymmetric couplings

In the limit of a small thermal bias $\Delta T \ll T$ (and arbitrary voltage bias), the thermocurrent in Eq. (S6) can be approximated as

$$\begin{aligned} I_{\text{th}} = & \gamma \int d\omega [f_L^{T+\Delta T}(\omega) - f_R^T(\omega)] A(\omega, V, T, B, \Delta T) \\ & - \gamma \int d\omega [f_L^T(\omega) - f_R^T(\omega)] A(\omega, V, T, B, \Delta T = 0) \end{aligned} \quad (\text{S9})$$

$$\begin{aligned} \approx & \gamma \int d\omega \Delta T \left(\frac{\partial f_L^{T+\Delta T}(\omega)}{\partial \Delta T} \right)_{\Delta T=0} A(\omega, V, T, B, \Delta T = 0) \\ & + \gamma \int d\omega \Delta T [f_L^T(\omega) - f_R^T(\omega)] \left(\frac{\partial A(\omega, V, T, B, \Delta T)}{\partial \Delta T} \right)_{\Delta T=0}, \end{aligned} \quad (\text{S10})$$

where we have omitted the arguments V, T and B of I_{th} for simplicity of notation and we have expanded the Fermi function $f_L^{T+\Delta T}(\omega)$ and the spectral function $A(\omega, V, T, B, \Delta T)$ to

order ΔT . Using,

$$\left(\frac{\partial f_L^{T+\Delta T}(\omega)}{\partial \Delta T} \right)_{\Delta T=0} = \frac{\omega - \mu_L}{T} \left(-\frac{\partial f_L^{T+\Delta T}(\omega)}{\partial \omega} \right)_{\Delta T=0} = \frac{\omega - \mu_L}{T} \left(-\frac{\partial f_L^T(\omega)}{\partial \omega} \right),$$

we have,

$$I_{\text{th}} = \frac{\gamma \Delta T}{T} \int d\omega (\omega - \mu_L) \left(-\frac{\partial f_L^T(\omega)}{\partial \omega} \right) A(\omega, V, T, B, \Delta T = 0) + \gamma \Delta T \int d\omega [f_L^T(\omega) - f_R^T(\omega)] \left(\frac{\partial A(\omega, V, T, B, \Delta T)}{\partial \Delta T} \right)_{\Delta T=0}, \quad (\text{S11})$$

$$\equiv I_{\text{th}}^a + I_{\text{th}}^b \quad (\text{S12})$$

The above equation is valid for $\Delta T \ll T$ and arbitrary V , however, we are mainly interested in explaining the experimentally observed field induced sign change in the slope of the thermocurrent with respect to V around $V = 0$ at low temperatures $\Delta T \ll T \ll T_K$ within the approach of Sec. SM.3.5. Further restricting to $\Delta T \ll T \ll T_K$, a Sommerfeld expansion of the first term, $I_{\text{th}}^a/\Delta T$, yields to lowest order in T ,

$$I_{\text{th}}^a = \frac{\gamma \Delta T}{T} \int d\omega (\omega - \mu_L) \left(-\frac{\partial f_L^T(\omega)}{\partial \omega} \right) A(\omega, V, T, B, \Delta T = 0) \approx \frac{\gamma \Delta T}{T} \frac{\pi^2 (k_B T)^2}{3} \left(\frac{\partial A(\omega, V, T = 0, B, \Delta T = 0)}{\partial \omega} \right)_{\omega=\mu_L} \quad (\text{S13})$$

$$\equiv \gamma \frac{\pi^2 k_B^2}{3} T \Delta T s(\omega = \mu_L, V, T = 0, B), \quad (\text{S14})$$

where $s(\omega = \mu_L, V, T = 0, B)$ in (S14) denotes the derivative of the $T = 0$ spectral function at $\omega = \mu_L$ on the RHS of (S13). Expanding $s(\omega = \mu_L, V, T = 0, B)$ in powers of V , i.e., $s(\omega = \mu_L, V, T = 0, B) = s_0(B) + \tilde{s}_1(B)V + \dots$, gives

$$I_{\text{th}}^a \approx \gamma \frac{\pi^2 k_B^2}{3} T \Delta T [s_0(B) + \tilde{s}_1^a(B)V + \dots]. \quad (\text{S15})$$

The second term in Eq. (S10) also gives a contribution to the thermocurrent which is linear in V, T and ΔT for $\Delta T \ll T \ll T_K$,

$$I_{\text{th}}^b = \gamma \Delta T \int d\omega [f_L^T(\omega) - f_R^T(\omega)] \left(\frac{\partial A(\omega, V, T, B, \Delta T)}{\partial \Delta T} \right)_{\Delta T=0} \quad (\text{S16})$$

$$\approx \gamma \Delta T \frac{\pi^2 k_B^2}{3} [\tilde{s}_1^b(B)TV + \dots], \quad (\text{S17})$$

which defines $\tilde{s}_1^b(B)$. The total thermocurrent $I_{\text{th}} = I_{\text{th}}^a + I_{\text{th}}^b$ is given by

$$I_{\text{th}}(\Delta T, V, T, B) \approx \gamma \frac{\pi^2 k_B^2}{3} T \Delta T [s_0(B) + s_1(B)V + \dots], \quad (\text{S18})$$

where $s_1(B) = \tilde{s}_1^a(B) + \tilde{s}_1^b(B)$. For $V \ll T_K$ and $\Delta T \ll T \ll T_K$, explicit expressions for $s_0(B)$ and $s_1(B)$ will be obtained below within higher-order Fermi-liquid theory and evaluated numerically exactly within the NRG.

Finally, we note that for $V = 0$, the second term in Eq. (S10) vanishes, and the first term reduces to the expected linear response thermocurrent ($\Delta T \ll T$ finite),

$$I_{\text{th}}(\Delta T, V = 0, T, B) = G(T, B)S(T, B)\Delta T, \quad (\text{S19})$$

where $G(T, B)$ and $S(T, B)$ are the linear conductance and linear Seebeck coefficient, respectively.

SM.3.5. Nonlinear thermocurrent and dI/dV : higher-order Fermi-liquid theory and NRG calculations

In order to evaluate the nonlinear thermocurrent in Eq. (S18) to order V , and hence $(\partial I_{\text{th}}(V)/\partial V)_{V=0}$, the spectral function $A(\omega, V, T, B) = \sum_{\sigma} A_{\sigma}(\omega, V, T, B)$ is required to order ω^2, V^2 and T^2 [see Eq. (S13)]. Moreover, this is required for the case of asymmetric lead couplings $\Gamma_L \ll \Gamma_R$, as is relevant to the molecular junction in the experiment (the case $\Gamma_L \gg \Gamma_R$ will also be considered). This can be obtained from the expression for the local level retarded self-energy of the quantum dot, $\Sigma_{\sigma}^r(\omega, V, T, B)$, to order ω^2, V^2 and T^2 from Ref. 7. Substitution of this into the expression for the spectral function,

$$A_{\sigma}(\omega, V, T, B) = -\frac{1}{\pi} \text{Im} \left[\frac{1}{\omega - \varepsilon_{0\sigma} + i(\Gamma_L + \Gamma_R) - \Sigma_{\sigma}^r(\omega, V, T, B)} \right], \quad (\text{S20})$$

yields, after some algebra,

$$\begin{aligned} \pi \Gamma A_{\sigma}(\omega, V, T, B) = & a_{0\sigma} + a_{1\sigma} \frac{\omega}{T_K} + a_{2\sigma} \left(\frac{\omega}{T_K} \right)^2 \\ & + a_{3\sigma} \left[(\beta_0 + 3\alpha^2) \left(\frac{V}{T_K} \right)^2 + \pi^2 \left(\frac{T}{T_K} \right)^2 \right] \\ & + a_{4\sigma} \alpha \frac{V}{T_K} + 2a_{5\sigma} \alpha \frac{V\omega}{T_K^2}, \end{aligned} \quad (\text{S21})$$

where T_K is defined via the $T = 0$ static spin susceptibility

$$\chi_s(T = 0) = (g\mu_B)^2 / 4k_B T_K, \quad (\text{S22})$$

the (field-dependent) coefficients $a_{i\sigma}$, $i = 0, \dots, 5$ will be defined below, and the constants β_0 and α are related to the lead couplings and to how the bias voltage drops across the leads [7],

$$\beta_0 = \frac{3\Gamma_L\Gamma_R}{(\Gamma_L + \Gamma_R)^2}, \quad (\text{S23})$$

$$\alpha = \frac{\alpha_L\Gamma_L - \alpha_R\Gamma_R}{\Gamma_L + \Gamma_R}. \quad (\text{S24})$$

The expression (S21) generalizes that in Ref. 7 [Eq.(5.4) therein] to arbitrary lead couplings and arbitrary voltage drops across the leads, and reduces to that in the limit of both a symmetric coupling to the leads ($\Gamma_L = \Gamma_R$) and a symmetric voltage drop across the leads ($\alpha_L = \alpha_R = \pm 1/2$). For the usual situation encountered in quantum dots, in which the voltage drop across the leads is symmetric, i.e., for $\alpha_L = \alpha_R = \pm 1/2$, we have that $\beta_0 + 3\alpha^2 = 3/4$, independent of the value of the lead couplings $\Gamma_{\alpha=L,R}$. Hence, the prefactor of the V^2 term in the spectral function (S21) also becomes independent of the lead couplings. The dependence on the latter, then only enters explicitly in (S21) via the terms proportional to αV and $\alpha V\omega$. For molecular quantum dots, such as those we address in this paper, the lead coupling asymmetry is large and α is therefore finite. In this case, the terms proportional to αV and $\alpha V\omega$ in Eq. (S21) need to be taken into account in calculating dI/dV and I_{th} up to the specified order in V and T .

The explicit expressions for the (field-dependent) coefficients $a_{i\sigma}$, $i = 0, \dots, 5$ appearing in Eq. (S21), read

$$a_{0\sigma} = \sin^2(\delta_\sigma), \quad (\text{S25})$$

$$a_{1\sigma} = \pi T_K \sin(2\delta_\sigma) \chi_{\sigma\sigma}, \quad (\text{S26})$$

$$a_{2\sigma} = (\pi T_K)^2 \left[\cos(2\delta_\sigma) (\chi_{\sigma\sigma}^2 + \frac{1}{2} \chi_{\uparrow\downarrow}^2) - \frac{\sin(2\delta_\sigma)}{2\pi} \frac{\partial \chi_{\sigma\sigma}}{\partial \varepsilon_{0\sigma}} \right] = a_{2\sigma}^{(2)} + a_{2\sigma}^{(3)}, \quad (\text{S27})$$

$$a_{3\sigma} = \frac{(\pi T_K)^2}{3} \left[\frac{3}{2} \cos(2\delta_\sigma) \chi_{\uparrow\downarrow}^2 - \frac{\sin(2\delta_\sigma)}{2\pi} \frac{\partial \chi_{\uparrow\downarrow}}{\partial \varepsilon_{0,-\sigma}} \right] = a_{3\sigma}^{(2)} + a_{3\sigma}^{(3)}, \quad (\text{S28})$$

$$a_{4\sigma} = 2\pi T_K \sin(2\delta_\sigma) \chi_{\uparrow\downarrow}, \quad (\text{S29})$$

$$a_{5\sigma} = (\pi T_K)^2 \left[\cos(2\delta_\sigma) (\chi_{\sigma\sigma} \chi_{\uparrow\downarrow} - \frac{1}{2} \chi_{\uparrow\downarrow}^2) - \frac{\sin(2\delta_\sigma)}{2\pi} \frac{\partial \chi_{\uparrow\downarrow}}{\partial \varepsilon_{0\sigma}} \right] = a_{5\sigma}^{(2)} + a_{5\sigma}^{(3)}, \quad (\text{S30})$$

where the static susceptibilities $\chi_{\sigma\sigma'}(T) = \int_0^{1/T} d\tau \langle \delta n_{0\sigma}(\tau) \delta n_{0\sigma'}(0) \rangle$, with $\delta n_{0\sigma}(\tau) = n_{0\sigma}(\tau) - \langle n_{0\sigma}(\tau) \rangle$, their derivatives, as well as the phase shifts, $\delta_\sigma = \pi n_{0\sigma}$, are evaluated at $T = 0$.

The latter can all be calculated, essentially exactly, within the NRG approach [10]. For later convenience, we also define $a_i = \sum_{\sigma} a_{i\sigma}$.

The meaning of the different terms in (S25)-(S30) is as follows: terms involving static susceptibilities $\chi_{\sigma_2, \sigma_3}$ describe two-body fluctuations (denoted as $a_{i\sigma}^{(2)}$), whereas those involving the nonlinear static susceptibilities $\chi_{\sigma_1 \sigma_2 \sigma_3}^3 = \partial \chi_{\sigma_2 \sigma_3} / \partial \varepsilon_{0\sigma_1}$ describe three-body fluctuations (denoted as $a_{i\sigma}^{(3)}$) [7]. The competition between the two- and three-body terms ultimately drives the splitting of the Kondo resonance in dI/dV at the field B_c (next section), as recently demonstrated for carbon nanotube quantum dots in the $SU(2)$ Kondo regime [28]. As will become evident below, the same competition accounts for the observed sign change of the zero-bias thermocurrent slope at $B_{th} \approx B_c$ for the molecular quantum dot in the main text.

SM.3.5.1. Splitting of the Kondo resonance in dI/dV and A

Before presenting results for the thermocurrent, it is useful to summarize the understanding of the splitting of the Kondo resonance in dI/dV and in the spectral function within the above higher-order (microscopic) Fermi-liquid theory [7]. Similar results can be obtained within an extension of the phenomenological Fermi-liquid theory for the Kondo model [29] to the Anderson model away from particle-hole symmetry [23, 30].

Consider first the differential conductance $G = dI/dV$. Substituting the spectral function from Eq. (S21) into the expression for the current (at $\Delta T = 0$) in Eq. (S4), and evaluating $G = dI/dV$, yields to order V^2 and T^2 [31]

$$G = \frac{dI}{dV} = g_0 \left[a_0 - c_T \pi^2 \left(\frac{T}{T_K} \right)^2 - c \frac{V}{T_K} - c_V \left(\frac{V}{T_K} \right)^2 \right], \quad (\text{S31})$$

where g_0 is given by

$$g_0 = G_0 \frac{2\Gamma_L \Gamma_R}{(\Gamma_L + \Gamma_R)^2},$$

and the curvature coefficients c_T and c_V and the coefficient c of the linear voltage term are given by,

$$c_T = -\frac{1}{3}(a_2 + 3a_3), \quad (\text{S32})$$

$$c_V = -\left[\frac{1}{4}a_2 + 3(\beta_0 + 3\alpha^2)a_3 \right] \rightarrow -\frac{1}{4}(a_2 + 9a_3), \quad (\text{S33})$$

$$c = -2\alpha a_4. \quad (\text{S34})$$

The second expression for c_V in (S33) is that for a symmetric voltage drop across the leads ($\alpha_L = \alpha_R = \pm 1/2$). For both a symmetric voltage drop across the leads ($\alpha_L = \alpha_R = \pm 1/2$) and equal lead couplings ($\Gamma_L = \Gamma_R$), i.e., for $\alpha = 0$, the results of Ref. 7 are recovered (note that due to slightly different definitions, our $c_{T,V}$ differ from those in Eq. (5.12) of Ref. 7 by a factor of 2).

The splitting of the Kondo resonance in dI/dV with increasing magnetic field can be formulated precisely in the case where the resonance lies at $V = 0$, i.e., when the coefficient, $c = -2\alpha a_4$, of the linear voltage term in (S34) vanishes. This is the case, either at particle-hole symmetry (mid-valley gate voltage), when $a_4 = 0$, or when the voltage drop across the leads is symmetric ($\alpha_L = \alpha_R = \pm 1/2$) and the lead couplings are equal ($\Gamma_L = \Gamma_R$). In these cases, a splitting in $G(V, T = 0, B)$ versus V upon increasing B occurs when a local maximum in this function for $B = 0$ at $V = V_0 = 0$ turns into a local minimum upon increasing B , i.e., when the curvature coefficient c_V changes sign at some field $B = B_V$. Similarly, a splitting in $G(V = 0, T, B)$ versus T upon increasing B occurs when a local maximum in this function for $B = 0$ at $T = T_0 = 0$ turns into a local minimum upon increasing B , i.e., when the curvature coefficient c_T changes sign at some field $B = B_T$.

In all other situations, the “zero-bias” peak in dI/dV , just like the Kondo resonance in the spectral function, will not lie exactly at $V = 0$ (or $\omega = 0$, in the case of the spectral function) [32]. For these cases we shall follow convention and simply define the splitting to occur as above, namely at the fields where the corresponding curvature coefficients change sign. We expect that this definition is reasonable deep in the Kondo regime where the Kondo resonance is pinned to within a fraction of T_K around $V = 0$ in dI/dV (or a fraction of T_K around $\omega = 0$ in the spectral function).

The splitting of the Kondo resonance in the spectral function can be described in an analogous manner to that above for dI/dV . For this purpose, we write the total spectral function, $A(\omega, V, T, B) = \sum_{\sigma} A_{\sigma}(\omega, V, T, B)$, in a similar way to that in (S31) for dI/dV :

$$\begin{aligned} \pi \Gamma A(\omega, V, T, B) = & a_0 + a_1 \frac{\omega}{T_K} - \bar{c}_{\omega} \left(\frac{\omega}{T_K} \right)^2 - \bar{c}_V \left(\frac{V}{T_K} \right)^2 - \bar{c}_T \pi^2 \left(\frac{T}{T_K} \right)^2 \\ & + \alpha a_4 \frac{V}{T_K} + 2\alpha a_5 \frac{V\omega}{T_K^2}, \end{aligned} \quad (\text{S35})$$

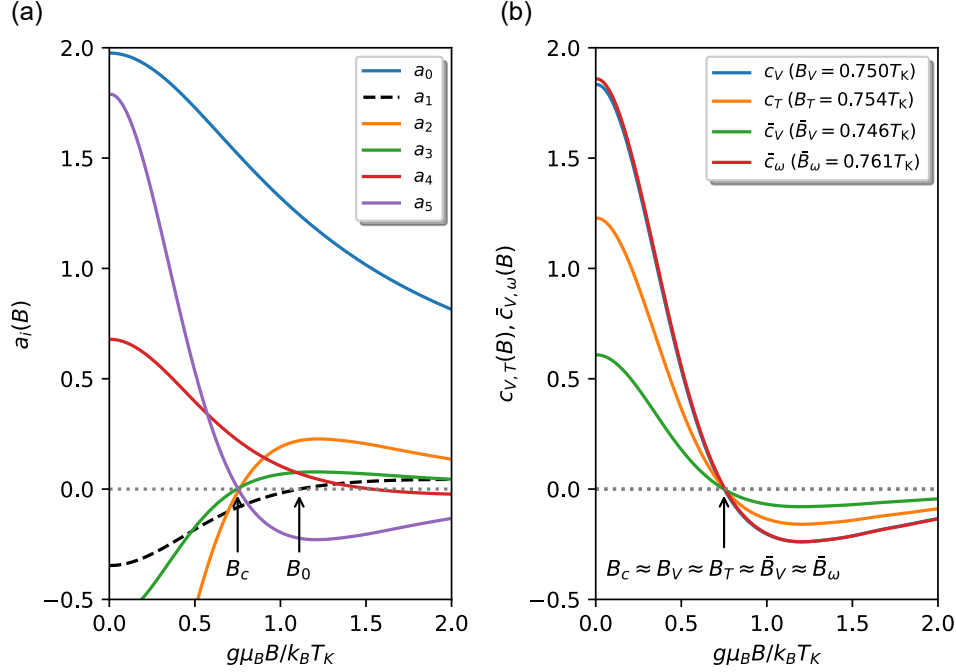


FIG. S10. NRG calculation of (a) the B -dependence of the coefficients $a_i = \sum_{\sigma} a_{i\sigma}$ appearing in the spectral function (S21), and, (b), the B -dependence of the curvature coefficients $c_V, c_T, \bar{c}_V, \bar{c}_\omega$ appearing in the spectral function ($\bar{c}_V, \bar{c}_\omega$) and in dI/dV (c_V, c_T). The coefficients a_2 and a_3 (and also a_5) enter the curvatures for the spectral function and dI/dV and change sign at $B_c \approx 0.75T_K$. All curvatures in (b) change sign at approximately the same field $B_c \approx 0.75T_K$. The coefficient a_1 (dashed line) determines the sign of the $V = 0$ thermocurrent and changes sign at a gate-voltage dependent field $B_0(V_g) > B_c$ (here, for $V_g = -1$, $B_0(V_g = -1) \approx 1.11T_K$), see Sec. SM.3.5.5 and Refs. 19. The parameters used ($U = 8\Gamma$, $\varepsilon_0 = -5\Gamma$, $V_g = -1$) correspond to typical values for the Kondo regime. The NRG calculations used a discretization parameter $\Lambda = 4$ and z -averaging with $N_z=4$ [17].

where the curvature coefficients $\bar{c}_\omega, \bar{c}_V$ and \bar{c}_T are given by,

$$\bar{c}_\omega = -a_2, \quad (\text{S36})$$

$$\bar{c}_V = -(\beta_0 + 3\alpha^2)a_3, \quad (\text{S37})$$

$$\bar{c}_T = -a_3. \quad (\text{S38})$$

As with the splitting fields B_V and B_T for dI/dV , we similarly define analogous fields \bar{B}_V, \bar{B}_T and \bar{B}_ω for the spectral function (S35), as the fields where the curvature coefficients \bar{c}_V, \bar{c}_T

and \bar{c}_ω change sign [23].

We now estimate the splitting fields via the curvatures defined above. From Eqs. (S37)-(S38), the curvatures \bar{c}_V and \bar{c}_T are proportional, implying that $\bar{B}_V = \bar{B}_T$ [23]. The four independent curvatures c_V, c_T for dI/dV and $\bar{c}_V, \bar{c}_\omega$ for the spectral function, are calculated by evaluating the coefficients $a_i(B) = \sum_\sigma a_{i\sigma}(B)$ within the NRG approach for a typical parameter set in the Kondo regime. The results are shown in Fig. S10(a) for the coefficients $a_i(B)$ and in Fig. S10(b) for the curvatures. We see that all four curvatures change sign at approximately the same field $B_V \approx B_T \approx \bar{B}_V (= \bar{B}_T) \approx \bar{B}_\omega$ [7, 23], with the difference between these values lying at the one % level for $U/\Gamma = 8$ and decreasing for larger values of U/Γ . Hence, the splitting of the Kondo resonance (“zero-bias peak”) in dI/dV (vs V or T) and in the spectral function $A(\omega, V, T, B)$ (vs V, T or ω), occurs at essentially the same magnetic field. We denote this field by B_c . In terms of the definition of T_K in Eq. (S22), this field is estimated as $B_c \approx 0.75T_K$ [see Fig. S10(b)], consistent with estimates from Refs. 7 and 23 [the former found $B_c \approx 0.76T_K$ while the latter found $B_c \approx 0.75T_K$], and also with that found for the spectral function of the Kondo model $B_c/T_K^{\text{HWHM}} \approx 0.5$ [22], upon using $T_K^{\text{HWHM}} \approx 1.5T_K$ (see Sec. SM.3.2).

The near exact coincidence of the splitting field for the various curvatures is ultimately due to the universality of the coefficients a_2, a_3 (and a_5) in the Kondo regime, where one can observe, to within around one % accuracy for $U/\Gamma = 8$, that

$$a_2 \approx 3a_3 \approx -a_5 \quad (\text{Kondo regime}), \quad (\text{S39})$$

with equality setting in for $U/\Gamma \rightarrow \infty$. Thus, any linear combination of these (such as the curvatures), scaled by their $B = 0$ value, results, to within the same accuracy, in a single universal function of B/T_K which changes sign at the universal field B_c . This is illustrated in Fig. S11(a). The two- and three-body contributions to the curvature c_V are also shown in Fig. S11(b) as a function of magnetic field, demonstrating the statement made at the end of Sec. SM.3.5, that the competition between these contributions drives the splitting of the Kondo resonance in dI/dV . Indeed, the three-body contributions contribute maximally at $B = B_c$.

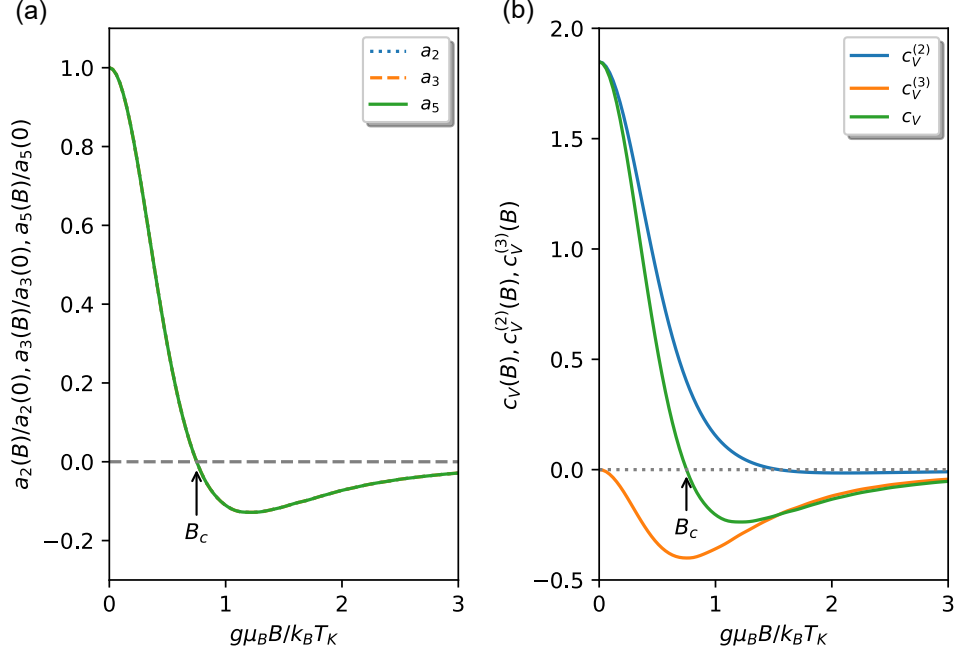


FIG. S11. (a) The B -dependence of the normalized coefficients $a_2(B)/a_2(0)$, $a_3(B)/a_3(0)$ and $a_5(B)/a_5(0)$ appearing in the spectral function (S21). (b) The B -dependence of the curvature coefficient c_V and its two- and three-body contributions, $c_V^{(2)}$ and $c_V^{(3)}$, respectively. The parameters used ($U = 16\Gamma$, $\varepsilon_0 = -7\Gamma$, $V_g = -1$) correspond to typical values for the asymmetric Kondo regime. NRG parameters as in Fig. S10.

SM.3.5.2. Experimental estimates of the splitting field B_c

Experiments which attempt to verify the result $g\mu_B B_c/k_B T_K^{\text{HWHM}} \approx 0.5$ (or, equivalently, $g\mu_B B_c/k_B T_K \approx 0.75$) by analyzing dI/dV data [33–38] have so far been hampered by the intrinsic problem of extracting B_c from dI/dV data [discussed in the main text in connection with Figs. 2(e)-2(f)], and by the absence of good estimates for T_K^{HWHM} in terms of the more usual scale used in quantum dots, that from the conductance $T_K^G \approx T_K$. This has resulted in estimates for $g\mu_B B_c/k_B T_K$ varying from 0.5 to 1.5 [38]. With the precise relation between these different scales, as discussed in Sec. SM.3.2, it may be possible to obtain more precise estimates of B_c . Nevertheless, recent high precision measurements analyzing dI/dV data and working with a certain Kondo scale T'_K , find $g\mu_B B_c/k_B T'_K = 0.23$ whereas that extracted from their $c_V(B_c) = 0$ yields instead $g\mu_B B_c/k_B T'_K = 0.38$, values which are inconsistent by 65% [28]. While these measurements were precise, the carbon nanotube quantum dot

investigated in this study might not be the best system to access Kondo universality, since level spacings are small and may invalidate the use of a single level Anderson model. Clearly, one needs both an appropriate system that is in the strongly correlated Kondo regime with $U/\Gamma \gg 1$ (compared to the typical value $3 - 4$ of carbon nanotube and semiconductor quantum dots) and an alternative to dI/dV measurements in order to reliably detect the onset of the splitting of the Kondo resonance. We show in the following section, that this alternative is provided by thermocurrent spectroscopy for molecular quantum dots. Since the latter generally have very large charging energies, with U/Γ of order $20 - 100$, accessing the universal splitting on the basis of a single level Anderson model is also expected to be more reliable than for semiconductor or carbon nanotube quantum dots.

SM.3.5.3. Thermocurrent $I_{\text{th}}(V)$ versus V in the Fermi-liquid regime

We now consider the thermocurrent within the above higher-order Fermi-liquid theory. This yields results valid for $V \ll T_K$ and $\Delta T \ll T \ll T_K$. Substituting the derivative of the spectral function at $\omega = \mu_L = \alpha_L V$ from Eq. (S21)

$$\left(\frac{\partial A(\omega, V, T=0, B, \Delta T=0)}{\partial \omega} \right)_{\omega=\mu_L} = \frac{1}{\pi \Gamma T_K} a_1 + \frac{1}{\pi \Gamma T_K^2} (2a_2 \alpha_L V + 2a_5 \alpha V) \quad (\text{S40})$$

into the first term of the expression for the thermocurrent in Eq. (S10) yields, assuming a symmetric voltage drop across the leads ($\alpha_L = \alpha_R = -1/2$) and a lead coupling asymmetry $\Gamma_L/\Gamma_R = \lambda$, noting that $2\alpha = (1 - \lambda)/(1 + \lambda)$,

$$I_{\text{th}}^a(V) = \gamma \frac{\pi^2 k_B^2 T}{3} \frac{\Delta T}{\pi \Gamma T_K} a_1 + \gamma \frac{\pi^2 k_B^2 T V}{3} \frac{\Delta T}{\pi \Gamma T_K^2} \left[\frac{1 - \lambda}{1 + \lambda} a_5 - a_2 \right]. \quad (\text{S41})$$

In order to evaluate the second term in Eq. (S10), i.e., I_{th}^b in Eq. (S16), we require the ΔT -dependence of the spectral function $A(\omega, T, V, B, \Delta T)$. For the molecular quantum dot in the experiment, a highly asymmetric coupling to the leads is found. Thus we only need to consider the two cases $\Gamma_L \ll \Gamma_R$ and $\Gamma_L \gg \Gamma_R$. In the former, the molecular quantum dot couples strongly to the right (cold) lead which is at temperature $T_R = T$ and the Kondo resonance is pinned to the chemical potential of the right lead. Hence, its temperature dependence is determined by $T_R = T$. In this case, the spectral function has a negligible dependence on ΔT for ω in the relevant transport window $[\mu_L, \mu_R] = [-V/2, +V/2]$, i.e. $(\partial A / \partial \Delta T) = 0$, so that $I_{\text{th}}^b \approx 0$. In the second case when the molecular quantum dot

couples strongly to the left (hot) lead, which is at temperature $T_L = T + \Delta T$, the Kondo resonance is pinned to the chemical potential of the left lead and its temperature dependence is determined by $T_L = T + \Delta T$ and will therefore be dependent on ΔT . In the Fermi liquid regime, this dependence will be given by Eq. (S35) with T replaced by $T_L = T + \Delta T$. We find using Eq. (S35),

$$(\partial A / \partial \Delta T)_{\Delta T=0} = (\partial A / \partial T_L)_{T_L=T} = -(1/\pi\Gamma)\bar{c}_T\pi^2 2T/T_K^2. \quad (\text{S42})$$

Substituting this into Eq. (S16), using $\bar{c}_T = -a_3$ [Eq. (S38)], gives for $\Gamma_L \gg \Gamma_R$,

$$I_{\text{th}}^b(V) = \gamma \frac{\pi^2 k_B^2 TV}{3} \frac{\Delta T}{\pi \Gamma T_K^2} [-6a_3]. \quad (\text{S43})$$

Thus, the total thermocurrent $I_{\text{th}} = I_{\text{th}}^a + I_{\text{th}}^b$ for $V \ll T_K$ and $\Delta T \ll T \ll T_K$ is given by,

$$I_{\text{th}}(V) = \gamma \frac{\pi^2 k_B^2 T}{3} \frac{\Delta T}{\pi \Gamma T_K} a_1 + \begin{cases} \gamma \frac{\pi^2 k_B^2 TV}{3} \frac{\Delta T}{\pi \Gamma T_K^2} \left[\frac{1-\lambda}{1+\lambda} a_5 - a_2 \right], & \text{if } \lambda = \Gamma_L/\Gamma_R \ll 1, \\ \gamma \frac{\pi^2 k_B^2 TV}{3} \frac{\Delta T}{\pi \Gamma T_K^2} \left[\frac{1-\lambda}{1+\lambda} a_5 - a_2 - 6a_3 \right], & \text{if } \lambda = \Gamma_L/\Gamma_R \gg 1, \end{cases} \quad (\text{S44})$$

i.e.,

$$I_{\text{th}}(V) \approx \gamma \frac{\pi^2 k_B^2}{3} T \Delta T [s_0(B) + s_1(B)V], \quad (\text{S45})$$

where $s_0(B)$ and $s_1(B)$ are given by,

$$s_0(B) = \frac{1}{\pi \Gamma T_K} a_1, \quad (\text{S46})$$

$$s_1(B) = \frac{1}{\pi \Gamma T_K^2} \begin{cases} \left[\frac{1-\lambda}{1+\lambda} a_5 - a_2 \right], & \text{if } \lambda = \Gamma_L/\Gamma_R \ll 1, \\ \left[\frac{1-\lambda}{1+\lambda} a_5 - a_2 - 6a_3 \right], & \text{if } \lambda = \Gamma_L/\Gamma_R \gg 1. \end{cases} \quad (\text{S47})$$

Using the aforementioned proportionalities $a_2 \approx 3a_3 \approx -a_5$ (valid deep in the Kondo regime), we find for the zero bias thermocurrent slope $(\partial I_{\text{th}}/\partial V)_{V=0} \propto s_1(B)$, for highly asymmetric lead couplings $\lambda \rightarrow 0$ and $\lambda \rightarrow \infty$,

$$s_1(B) = \begin{cases} \frac{1}{\pi \Gamma T_K^2} [+a_5 - a_2] \approx -\frac{2a_2}{\pi \Gamma T_K^2}, & \text{if } \lambda = \Gamma_L/\Gamma_R \ll 1, \\ \frac{1}{\pi \Gamma T_K^2} [-a_5 - a_2 - 6a_3] \approx -\frac{2a_2}{\pi \Gamma T_K^2}, & \text{if } \lambda = \Gamma_L/\Gamma_R \gg 1. \end{cases} \quad (\text{S48})$$

i.e., for highly asymmetric lead couplings, the thermocurrent slope in the Kondo regime is independent of whether the molecule couples strongly to the left (hot) or right (cold) lead.

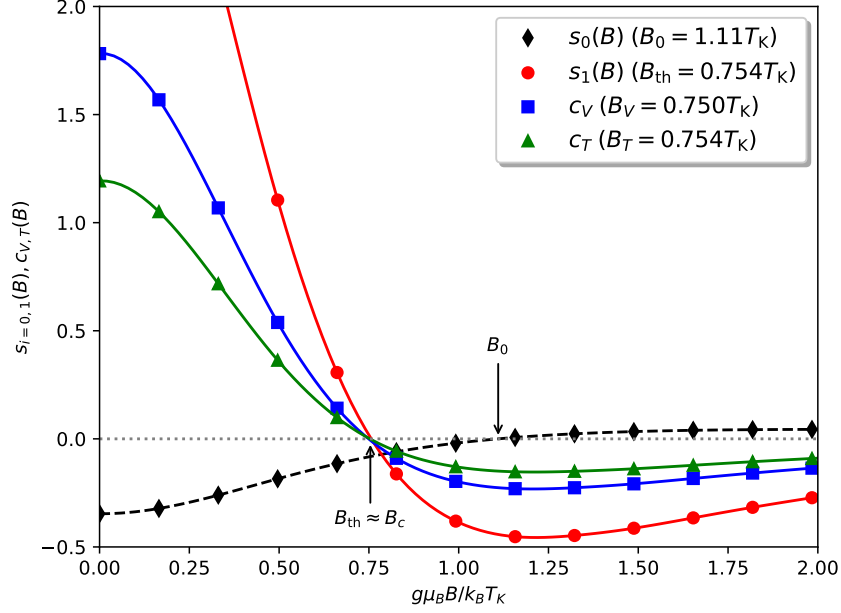


FIG. S12. NRG calculations for the B -dependence of the coefficients s_0 and s_1 appearing in the low temperature thermocurrent Eq (S45) [for $\lambda = \Gamma_L/\Gamma_R \rightarrow 0$ and dropping the prefactors $1/\pi\Gamma T_K$ and $1/\pi\Gamma T_K^2$], and compared to the B -dependence of the coefficients c_V and c_T appearing in the low temperature differential conductance. The coefficient $s_1(B)$, and hence the slope of $I_{\text{th}}(V)$ at $V = 0$, changes sign at $B = B_{\text{th}} \approx 0.754T_K$ close to the value at which c_V and c_T in the differential conductance change sign. In contrast, the sign of the $V = 0$ thermocurrent, determined by $s_0(B)$, changes sign at a higher field $B_0(V_g = -1) \approx 1.11T_K > B_{\text{th}} \approx B_c$ (see Sec. SM.3.5.5 and Refs. 19). Parameters typical for the asymmetric Kondo regime are used: $U/\Gamma = 8$, $\varepsilon_0 = -5\Gamma$, $V_g = -1$. NRG parameters as in Fig. S10.

The dependence of $s_1(B)$ on the coupling asymmetry λ is weak and enters through the prefactor of the a_5 coefficient in Eq. (S47).

Equation (S45) describes the leading temperature and voltage corrections to the nonlinear thermocurrent valid for $T, V \ll T_K$, asymmetric lead couplings, and arbitrary magnetic field B . It allows us to address the experimentally observed sign change of $(\partial I_{\text{th}}(V)/\partial V)_{V=0} \propto s_1(B)$ upon increasing B above B_{th} and also to determine the value of B_{th} . The field-dependence of the coefficients $a_i, i = 0, \dots, 5$, evaluated within the NRG for a typical parameter set in the Kondo regime, were shown above in Fig. S10. In Fig. S12 we show the B -dependence of the coefficients $s_0(B)$ and $s_1(B)$. For comparison, the field-dependence of

the curvature coefficients c_T and c_V of dI/dV are also shown. Remarkably, we find that $s_1(B)$ changes sign at essentially the same field at which the Kondo resonance splits in a magnetic field, i.e., $B_{\text{th}} = B_c$ (the deviation of B_{th} from B_c decreases, with increasing U , see next section). Moreover, deep in the Kondo regime, this value is largely independent of the lead coupling asymmetry λ due to the aforementioned proportionality of the coefficients a_5, a_2 and a_3 which all change sign at the same (universal) field [$B = B_c$, see Fig. S10(a)]. Thus, the sign change of the slope of the thermocurrent $(\partial I_{\text{th}}(V)/\partial V)_{V=0} \propto s_1(B)$ occurs at the splitting field B_c independent on the precise value of the lead coupling asymmetry. Thus, thermocurrent measurements of Kondo correlated quantum dots at finite bias voltage provide a new way to determine the splitting of the Kondo resonance, independent of the usual way via the differential conductance.

Finally, we note that while the first term in Eq. (S45), proportional to s_0 , is a linear response quantity [see Eqs. (S12), (S39) and (S31)], the second term, proportional to $s_1(B)$, and linear in V , is a nonequilibrium quantity, as it arises from contributions of $O(V\omega)$ to the spectral function [Eqs. (S35) and (S40)].

SM.3.5.4. Universal scaling functions for $s_1(B)$ and $c_V(B)$

The main text [Fig 4(a)] showed that for $U/\Gamma \gg 1$, $s_1(B)/s_1(0)$ and $c_V(B)/c_V(0)$ are universal scaling functions of their argument $(g\mu_B B/k_B T_K)$ in the Kondo regime of gate voltages V_g . The dependence of these functions on $U/\Gamma \gg 1$ for gate voltages close to mid-valley (i.e., in the Kondo regime) is shown in Fig. S13 for three different values of $U/\Gamma = 5, 8$ and 16 . One observes that the difference between these two functions decreases with increasing U/Γ (inset to Fig. S13), with the maximum absolute difference being below 2% for $U/\Gamma = 5$, below 0.6% for $U/\Gamma = 8$ and below 0.01% for $U/\Gamma = 16$. Hence, in the Kondo limit and for $U/\Gamma \gg 1$, the normalized scaling functions for the slope of the thermocurrent and the curvature coefficient of the differential conductance, while strictly different, can nevertheless be well approximated by a single scaling function. An approximate interpolation formula for this function, valid for a large range of $b = g\mu_B B/k_B T_K$ from $b \ll 1$ to $b \gg 1$, is given by

$$f_1(b) = \frac{(1 - \alpha_0 b^2)}{(1 + \beta_0 b^2)^z}, \quad (\text{S49})$$

where $\alpha_0 \approx 1.77, \beta_0 \approx 1.12$ and $z \approx 2.6$. This was used in the main text to fit the experimental data for the zero-bias thermocurrent slope to the above universal curve (see SM.1.4).

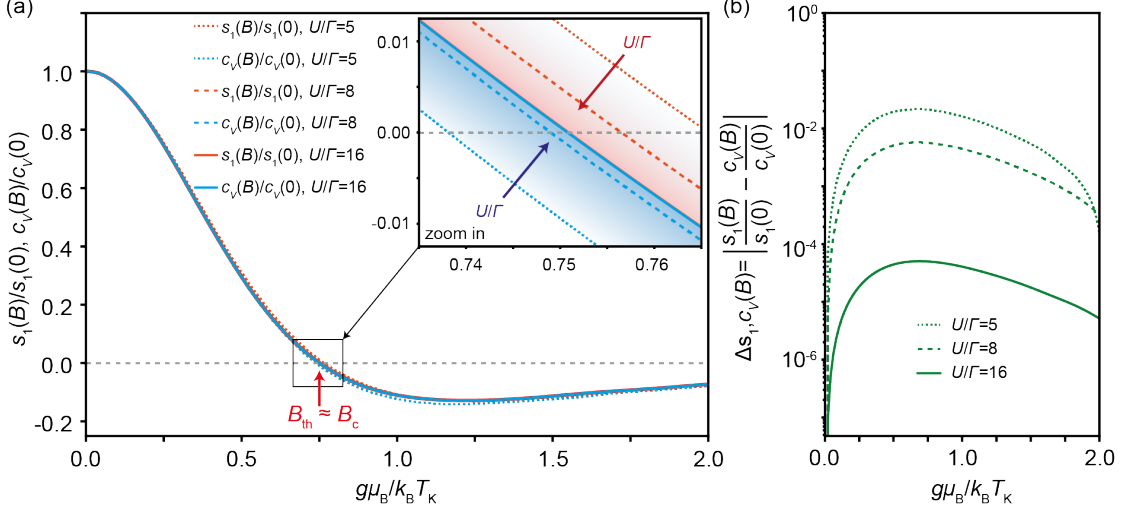


FIG. S13. (a) Scaling of the normalized zero-bias thermocurrent slope $\propto s_1(B)/s_1(0)$ (blue) and the normalized curvature coefficient $c_V(B)/c_V(0)$ (red) with increasing U/Γ for V_g in the Kondo regime ($V_g = 1$ for $U/\Gamma = 16$, $V_g = 1.5$ for $U/\Gamma = 8$ and $V_g = 0.5$ for $U/\Gamma = 5$). The inset shows the behaviour near $B_{th} \approx B_c$. (b) The absolute difference $\Delta_{s_1, c_V}(B) = \left| \frac{s_1(B)}{s_1(0)} - \frac{c_V(B)}{c_V(0)} \right|$ between the normalized s_1 and c_V versus B for $U/\Gamma = 5, 8$ and 16 . NRG parameters as in Fig. S10.

The above universality in c_V and s_1 follows, from the observation made previously that in the Kondo regime a_2, a_3 and a_5 are proportional to each other [Eq. (S39)], and when normalized by their $B = 0$ values, collapse onto the same universal curve for $U/\Gamma \gg 1$ [Fig. S11(a)]. Hence, any linear combination of these, such as c_V or s_1 , will also follow this curve and will also change sign at the universal field B_c . The same competition between two- and three-body fluctuations that drives the splitting of the Kondo resonance in dI/dV via the vanishing of c_V at $B = B_c$ [see Fig. S11(b)], is also responsible for the sign change of the zero-bias thermocurrent slope s_1 at $B = B_{th} \approx B_c$, i.e., the three-body fluctuations also play an important role for the thermocurrent.

Finally, one can summarize the universal aspects of magnetic field effects on the spectral function (through the coefficients a_2, a_3 and a_5), differential conductance (through the curvatures, themselves functions of a_2 and a_3) and the thermocurrent (through s_1 , a function

of a_2 and a_5) in the Kondo limit for $U/\Gamma \gg 1$ by a single function, approximately given by Eq. (S49). Deviations from this universality arise for weak correlations or outside the Kondo regime (e.g. on approaching the mixed-valence regime). In the latter case, the deviations result from particle-hole asymmetry and are described by the coefficients a_1 and a_4 , where a_1 (a_4) shifts the zero-energy (zero-bias) peak in $A(\omega)$ (dI/dV) to finite energy (voltage) [see Eqs. (S35) and (S31)], with a_1 also being responsible for the finite thermocurrent offset at $V = 0$ through the coefficient s_0 [see Eq. (S46)].

SM.3.5.5. Zero-bias thermocurrent and zero-bias thermocurrent slope

We contrast the above findings to the experiment of Svilans et al. in Ref 39. In this experiment, the gate-voltage (V_g) dependence of the zero-bias thermocurrent $I_{\text{th}}(V = 0, V_g) \propto s_0$ was measured, as a function of temperature and as a function of magnetic field for a range of gate voltages around mid-valley ($V_g = 0$). A sign change of $I_{\text{th}}(V = 0, V_g)$ and its $V_g = 0$ slope $(\frac{\partial I_{\text{th}}(V=0, V_g)}{\partial V_g})_{V_g=0}$ was observed upon increasing the magnetic field at low temperatures $T \lesssim T_K$.

The above observations can be understood from Eq. (S19), which shows that $I_{\text{th}}(V = 0, V_g) = G(T, B)S(T, B)\Delta T$ is a linear-response quantity, whose sign changes, as a function of temperature or magnetic field, are determined by sign changes of the linear Seebeck coefficient $S(T, B)$. Ref. 19, showed that the sign change in the zero-bias thermocurrent occurs at a gate-voltage dependent field $B_0(V_g) > B_c$. The sign change in the slope $(\frac{\partial I_{\text{th}}(V=0, V_g)}{\partial V_g})_{V_g=0}$ also occurs at $B_0(V_g = 0)$, as can be seen by expanding $I_{\text{th}}(V = 0, V_g)$ about $V_g = 0$,

$$I_{\text{th}}(V = 0, |V_g| \ll 1) = I_{\text{th}}(V = 0, V_g = 0) + V_g \left. \frac{\partial I_{\text{th}}(V, V_g)}{\partial V_g} \right|_{V_g=0} + \dots \quad (\text{S50})$$

and noting that, since $I_{\text{th}}(V = 0, V_g = 0) = 0$ by particle-hole symmetry, $I_{\text{th}}(V = 0, |V_g| \ll 1)$, and its derivative with respect to V_g , both change sign at the same field, i.e., at $B = B_0(|V_g| \ll 1)$. Indeed, Svilans et al. [39] commented on the fact that the experimental field at which the low temperature value of $(\frac{\partial I_{\text{th}}(V=0, V_g)}{\partial V_g})_{V_g=0}$ changes sign exceeds the expected field $B = B_c$ for the splitting. Equation (S50), together with the result $B_0(V_g \rightarrow 0) > B_c$ [19] explains this observation. For typical values of $U/\Gamma \gg 1$, $B_0(0)$ can be a factor two larger than B_c [19], hence, B_0 cannot be used to estimate the splitting field B_c .

In contrast to the non-universal zero-bias thermocurrent s_0 [see Fig. 4(a) of the main text]

and its slope with respect to V_g at $V_g = 0$, the zero-bias slope of the thermocurrent $\propto s_1(B)$ measured in the present experiment is universal and changes sign at the universal field $B_{\text{th}} \approx B_c$. Thus thermocurrent spectroscopy, via the slope of the zero-bias thermocurrent, is able to access universal aspects of Kondo physics. Non-universal aspects, such as the small finite offset of the zero bias thermocurrent $I_{\text{th}}(V = 0, V_g) \propto T\Delta T s_0(B)$ can, however, also be of some practical interest. In particular, the sign of this offset at $T \ll T_K$ and $B = 0$ measures the deviation from particle-hole symmetry for a given gate voltage V_g , and indicates whether the Kondo resonance lies above (for $V_g > 0$) or below (for $V_g < 0$) the Fermi level.

SM.3.5.6. Temperature and thermal bias effects

The higher-order Fermi-liquid theory suffices to capture the main observation of the experiment, i.e., the kink (slope change) in I_{th} vs V upon increasing B above B_c in the low-temperature strong coupling regime $\Delta T \ll T \ll T_K$. We comment briefly on the effect of increasing either temperature T or the thermal bias ΔT to values above T_K starting from the above regime, i.e., $B > B_c$ and $\Delta T \ll T \ll T_K$. Since increasing temperature increases the effective splitting field $B_c(T) > B_c(T = 0)$ [22], for sufficiently high temperature one will eventually be in the regime where $B < B_c(T)$ and the kink in I_{th} vs V at $V = 0$ will vanish. Similarly, increasing the thermal bias acts like increasing the effective base temperature $T \rightarrow T_{\text{eff}}(\Delta T) > T$, as noted in the experiment in Fig. S7, so again the kink will vanish for sufficiently large thermal bias. The vanishing of the kink in I_{th} vs V at $V = 0$ with increasing T or ΔT is, indeed, consistent with the measurements [see Figs. S4(a)-S4(b) and Figs. S5(a)-S5(b)]. In the next section, we quantify the above expectations for the temperature and thermal bias dependence of the nonlinear thermocurrent, by using an approximate method, which applies to a wider range of bias voltages, thermal biases and temperatures, than those accessible within the higher-order Fermi-liquid theory.

SM.3.6. Equation of motion method for nonlinear thermoelectric transport

In the strongly nonlinear regime, where V, T or ΔT become comparable to or larger than the low temperature scale T_K , we require a more generally applicable, albeit less exact, the-

ory of nonequilibrium thermoelectric transport through a Kondo-correlated quantum dot as compared to that offered by the NRG for linear transport [5, 19, 21, 40, 41], or the higher-order Fermi-liquid theory described above, which is valid for finite small $V, \Delta T \ll T \ll T_K$ [7, 8]. Here, we shall use the recently developed Green function equation of motion decoupling technique [11, 12], which generalizes an earlier approach of Lacroix [42] for the finite U Anderson impurity model in equilibrium to the two-lead Anderson model (S3) out of equilibrium. Within this approach, electrical transport out of equilibrium was investigated at $B = 0$ and at finite B for the symmetric case [11]. A first application of this technique to thermal transport, at zero magnetic field, investigated efficiency, power and generalized Seebeck coefficients at large thermal (ΔT) and voltage (V) biases of Kondo-correlated quantum dots [43][44]. Here, we go one step further and include a finite magnetic field B in order to investigate the field, temperature, voltage and thermal bias dependence of the thermocurrent I_{th} . We compare the results obtained with the corresponding measurements in the experiment.

SM.3.6.1. Equation of motion method and numerical calculations

Full details of the approach may be found elsewhere [11, 12], so here we shall only give a brief account. Starting with the local retarded Green function of the dot $G_{0\sigma}(\omega) = \langle\langle d_\sigma; d_\sigma^\dagger \rangle\rangle$, one considers its equation of motion (EOM),

$$(\omega - \varepsilon_{0\sigma})G_{0\sigma}(\omega) = 1 + \sum_{k\alpha} t_\alpha \langle\langle c_{k\alpha\sigma}; d_\sigma^\dagger \rangle\rangle + U \langle\langle n_{0,-\sigma} d_\sigma; d_\sigma^\dagger \rangle\rangle, \quad (\text{S51})$$

which results in two new Green functions on the RHS. The EOM for the first Green function $\langle\langle c_{k\alpha\sigma}; d_\sigma^\dagger \rangle\rangle$,

$$(\omega - \varepsilon_{k\alpha\sigma}) \langle\langle c_{k\alpha\sigma}; d_\sigma^\dagger \rangle\rangle = t_\alpha \langle\langle d_\sigma; d_\sigma^\dagger \rangle\rangle, \quad (\text{S52})$$

returns $G_{0\sigma}$, while the EOM of the second Green function, $\langle\langle n_{0,-\sigma} d_\sigma; d_\sigma^\dagger \rangle\rangle$, results in three new Green functions (see Refs. 11, 42, and 43). A closed set of equations can be obtained by writing down the EOM of the latter three Green functions and decoupling the resulting higher-order Green functions with two lead operators (e.g., of the kind $\langle\langle c_{k\alpha-\sigma}^\dagger c_{k'\alpha',-\sigma} d_\sigma; d_\sigma^\dagger \rangle\rangle$) in terms of mean fields $\langle d_\sigma^\dagger c_{k\alpha\sigma} \rangle$, $\langle c_{k\alpha\sigma}^\dagger c_{k'\alpha\sigma} \rangle$ and lower order Green

functions, e.g.,

$$\langle\langle c_{k\alpha,-\sigma}^\dagger c_{k'\alpha',-\sigma} d_\sigma; d_\sigma^\dagger \rangle\rangle \approx \langle c_{k\alpha,-\sigma}^\dagger c_{k'\alpha',-\sigma} \rangle \langle\langle d_\sigma; d_\sigma^\dagger \rangle\rangle, \quad (\text{S53})$$

$$\langle\langle d_{-\sigma}^\dagger c_{k'\alpha',-\sigma} c_{k\alpha,\sigma}; d_\sigma^\dagger \rangle\rangle \approx \langle d_{-\sigma}^\dagger c_{k'\alpha',-\sigma} \rangle \langle\langle c_{k\alpha,\sigma}; d_\sigma^\dagger \rangle\rangle. \quad (\text{S54})$$

This then allows one to obtain a closed expression for the dot Green function [12, 42]:

$$G_{0\sigma}(\omega) = \frac{1 + K_\sigma(\omega) [\langle n_{0,-\sigma} \rangle + \Sigma_{\sigma,4}(\omega)]}{\omega - \varepsilon_{0\sigma} - \Sigma_{\sigma,0}(\omega) + K_\sigma(\omega) [\Sigma_{\sigma,1}(\omega) - \Sigma_{\sigma,0}(\omega)\Sigma_{\sigma,4}(\omega)]}, \quad (\text{S55})$$

where the self-energies $\Sigma_{\sigma,i=0,\dots,4}(\omega)$ and $K_\sigma(\omega)$ (denoted by $I_\sigma(\omega)$ in [12]) are given by [12]

$$\Sigma_{\sigma,0}(\omega) = \sum_{k\alpha} \frac{t_\alpha^2}{\omega - \epsilon_{k\alpha}}, \quad (\text{S56})$$

$$\Sigma_{\sigma,1}(\omega) = \sum_{k\alpha} t_\alpha^2 \left[\frac{\sum_{k'} \langle c_{k\alpha,-\sigma}^\dagger c_{k'\alpha,-\sigma} \rangle}{\omega - (\varepsilon_{0\sigma} - \varepsilon_{0,-\sigma}) - \epsilon_{k\alpha} + i\gamma_\sigma} + \frac{\sum_{k'} \langle c_{k'\alpha,-\sigma}^\dagger c_{k\alpha,-\sigma} \rangle}{\omega - (\varepsilon_{0\sigma} + \varepsilon_{0,-\sigma} + U) + \epsilon_{k\alpha} + i\gamma_D} \right], \quad (\text{S57})$$

$$\Sigma_{\sigma,2}(\omega) = \sum_{k\alpha} t_\alpha^2 \left[\frac{1 - \sum_{k'} \langle c_{k\alpha,-\sigma}^\dagger c_{k'\alpha,-\sigma} \rangle}{\omega - (\varepsilon_{0\sigma} - \varepsilon_{0,-\sigma}) - \epsilon_{k\alpha} + i\gamma_\sigma} + \frac{1 - \sum_{k'} \langle c_{k'\alpha,-\sigma}^\dagger c_{k\alpha,-\sigma} \rangle}{\omega - (\varepsilon_{0\sigma} + \varepsilon_{0,-\sigma} + U) + \epsilon_{k\alpha} + i\gamma_D} \right], \quad (\text{S58})$$

$$\Sigma_{\sigma,3}(\omega) = \sum_{k\alpha} t_\alpha^2 \left[\frac{1}{\omega - (\varepsilon_{0\sigma} - \varepsilon_{0,-\sigma}) - \epsilon_{k\alpha} + i\gamma_\sigma} + \frac{1}{\omega - (\varepsilon_{0\sigma} + \varepsilon_{0,-\sigma} + U) + \epsilon_{k\alpha} + i\gamma_D} \right], \quad (\text{S59})$$

$$\Sigma_{\sigma,4}(\omega) = \sum_{k\alpha} t_\alpha \left[\frac{\langle d_{-\sigma}^\dagger c_{k\alpha,-\sigma} \rangle}{\omega - (\varepsilon_{0\sigma} - \varepsilon_{0,-\sigma}) - \epsilon_{k\alpha} + i\gamma_\sigma} - \frac{\langle c_{k\alpha,-\sigma}^\dagger d_{-\sigma} \rangle}{\omega - (\varepsilon_{0\sigma} + \varepsilon_{0,-\sigma} + U) + \epsilon_{k\alpha} + i\gamma_D} \right], \quad (\text{S60})$$

$$K_\sigma(\omega) = \frac{U}{\omega - \varepsilon_{0\sigma} - \Sigma_{\sigma,0}(\omega) - \Sigma_{\sigma,3}(\omega)}. \quad (\text{S61})$$

Within the Lacroix theory, the lifetime of the single particle (γ_σ) and doubly occupied (γ_D) states of the dot appearing in the denominators of the self-energies $\Sigma_{\sigma,1}, \dots, \Sigma_{\sigma,4}$ vanish, being given by the usual $i\delta = i0^+$ of retarded Green functions. Additional considerations, however, show that these have finite values [11, 12]. They are evaluated in perturbation theory for the finite U Anderson model to fourth order in t_α for γ_σ and to second order in t_α for γ_D and describe lifetime broadening due to finite B, T or V and generalize the results for the infinite U Anderson model [45]. The effect of γ_σ and γ_D is to cut off the logarithmic singularities in the self-energies at $\mu_{L,R} \pm g\mu_B B/2$ at low T . This in turn leads to several

improvements over the Lacroix theory in which $i\gamma_\sigma = i\gamma_D = i\delta = i0^+$. For example, the Kondo resonance at the particle-hole symmetric point ($2\varepsilon_0 + U = 0$), absent in the Lacroix theory, is recovered within this approach[11, 12]. Another improvement over the Lacroix theory concerns the exponent in the Kondo scale. Within this theory, $T_K \sim e^{\pi\varepsilon_0(\varepsilon_0+U)/(1.5\Gamma U)}$, which comes closer to the exact one, $T_K \sim e^{\pi\varepsilon_0(\varepsilon_0+U)/(2\Gamma U)}$, as compared to the Lacroix theory which gives $T_K \sim e^{\pi\varepsilon_0(\varepsilon_0+U)/(\Gamma U)}$ [11]. Moreover, the expected features of the nonequilibrium Kondo resonance, such as the peaks in the spectral function at the two chemical potentials $\mu_L = +eV/2$ and $\mu_R = -eV/2$ for $B = 0$, and the peaks at $\mu_{L,R} \pm g\mu_B B/2$ on applying a magnetic field, are also recovered [11, 43]. Hence, the approach captures the qualitative features of the nonequilibrium Kondo effect in a magnetic field and we therefore expect that the same will hold for the field and voltage dependent thermocurrent of interest to us here.

The expectation values $n_{0,-\sigma} = \langle d_{-\sigma}^\dagger d_{-\sigma} \rangle$, $\langle d_{-\sigma}^\dagger c_{k-\alpha\sigma} \rangle$ and $\langle c_{k\alpha,-\sigma}^\dagger c_{k'\alpha,-\sigma} \rangle$ appearing in the above equations can be related to the dot Green function $G_{0,-\sigma}$ in the wide band limit[11]. Hence, Eq.(S55) represents a set of two coupled integral equations relating $G_{0\uparrow}$ and $G_{0\downarrow}$. They reduce to a single integral equation for $G_{0\uparrow}(\omega) = G_{0\downarrow}(\omega)$ at zero magnetic field $|\varepsilon_{0\sigma} - \varepsilon_{0,-\sigma}| = |g\mu_B B| = 0$. The integral equations are solved self-consistently by numerical iteration subject to the constraint on the occupation numbers [12]

$$n_{0\sigma}(\omega) = \int d\omega f_{neq}(\omega, V, T) A_\sigma(\omega, V, T, B), \quad (\text{S62})$$

where $A_\sigma(\omega, V, T, B) = -\text{Im}[G_{0\sigma}(\omega + i\delta, V, T, B)]/\pi$ is the nonequilibrium spectral function of the dot[46] and $f_{neq}(\omega, V, T)$ is a nonequilibrium distribution function given by,

$$f_{neq}(\omega, V, T) = \frac{\Gamma_L f_L(\omega) + \Gamma_R f_R(\omega)}{\Gamma_L + \Gamma_R}. \quad (\text{S63})$$

In practice, the above theory suffers from a small violation of particle-hole symmetry [11]. This is negligible for $B = 0$, but needs to be corrected for finite field calculations. This is done by implementing particle-hole symmetry $H(\varepsilon_0, U, B, \mu_L, \mu_R) \leftrightarrow H(-(\varepsilon_0 + U), U, -B, \mu_R, \mu_L)$ explicitly. This requires solving two sets of coupled integral equations for $G_{0\uparrow}^{\varepsilon_0}, G_{0\downarrow}^{\varepsilon_0}$ and their particle-hole transformed pairs $G_{0\uparrow}^{-(\varepsilon_0+U)}, G_{0\downarrow}^{-(\varepsilon_0+U)}$ and symmetrizing at each iteration to maintain particle-hole symmetry [47]. Stable results are obtained at the cost of a slower convergence. We used adaptive integration routines with additional intervals for the regions around the points $\mu_{L,R} \pm g\mu_B B/2$ where the integrands of the self-energies (S57)-(S60) have a rapid variation. The calculations become feasible by distributing the integrations over 256

OpenMP threads on the JURECA supercomputer of Forschungszentrum Jülich (each node on this supercomputer has 2 AMD EPYC 7742 CPUs, and each CPU has 64 cores running at 2.25 GHz. With hyperthreading this gives 256 threads/node; 2 nodes were used in the calculations, one for $\Delta T = 0$ and one for $\Delta T > 0$). Our convergence criterion was that the Euclidean norm of the difference of successive iterates be less than 10^{-3} .

SM.3.6.2. Model parameters and ranges for V, B, T and ΔT

Since all the interesting effects in Kondo-correlated quantum dots occur on a scale of order T_K , the theoretical results are shown as functions of the dimensionless ratios $eV/k_B T_K$, $g\mu_B B/k_B T_K$, $\Delta T/T_K$. From experiment $T_K \approx 12.8K$ is extracted from the universal Kondo conductance curve via $G(T = T_K) = G(T = 0)/2$ so an experimental V -range from $-10mV$ to $+10mV$ would correspond to $eV/k_B T_K$ values up to $10 \times 0.001 \times 1.6 \times 10^{-19}/(1.38 \times 10^{-23} \times 12.8) = 9.055 \approx 10$, so using $-10 \leq eV/k_B T_K \leq +10$ corresponds closely to an experimental range $-10mV \leq V \leq +10mV$. The splitting of the Kondo resonance occurs at a field $g\mu_B B_c = 0.5k_B T_K^{\text{HWHM}} = 0.75k_B T_K$ where T_K^{HWHM} is the Kondo scale defined as the HWHM of the $T = 0$ Kondo resonance [22] and T_K , defined in Eq. (S22), is close the Kondo scale extracted from the conductance[21]. Hence, from $g\mu_B B_c = 0.75k_B T_K$ we find $B_c = 7.15$ T using $T_K = 12.8K$ and the measured $g = 2$ from EPR in Sec. SM.4.2. The sign change of the slope of I_{th} for $V \rightarrow 0$ in the main text occurs at $B \approx 6.6T$, which is within 10 per cent of the predicted $B_{\text{th}} \approx B_c$ within the higher-order Fermi-liquid theory.

The asymmetry ratio, $\Gamma_L/\Gamma_R = \lambda = 0.017$, extracted from the measured conductance in the main text was used for the calculations. The gate coupling for the device in the main text was weak (Fig. S8) so estimates for the charging energy and local level position ε_0 were not possible. However, the Kondo resonance in dI/dV has a marked asymmetry about $V = 0$, suggesting a level energy ε_0 in the asymmetric Kondo regime a few Γ away from the mixed valence regime, since in this case the spectral function shows the above kind of asymmetry. Taking $U/\Gamma = 8$, for example, one may reproduce the observed asymmetry in dI/dV by using $\varepsilon_0/\Gamma = -5$ or -5.5 . The precise values, are, however, not important for a description of the main trends in the thermocurrent that we wish to describe. The field range used for the device in the main text is $0 \leq g\mu_B B/k_B T_K \lesssim 0.85$, in the calculations we show a wider range $0 \leq g\mu_B B/k_B T_K \lesssim 4$ to illustrate more clearly the differences between the low and

high field behavior of I_{th} . In the experiments, temperature and thermal bias ranges were $0.16 \lesssim T/T_K \lesssim 1.2$ and $0.05 \lesssim \Delta T/T_K \lesssim 0.4$, respectively. We shall use $0.5 \leq T/T_K \leq 4$ and $0.2 \leq \Delta T/T_K \leq 3$ extending the higher end for these quantities, while ensuring that we also access values for these quantities in the strong coupling regime.

SM.3.6.3. Magnetic field dependence

Figs. 3(a) and 3(b) (main text) show the measured I_{th} vs B and V at a small thermal bias $\Delta T/T_K = 0.6/12.8 \approx 0.05$ and at a low base temperature $T/T_K = 2/12.8 \approx 0.16$, while Figs. 2(c) and 2(d) (main text) show the corresponding dI/dV . Calculations within the EOM approach described above, for finite B , become numerically intractable for $T \ll T_K$, and for too small a thermal bias $\Delta T \ll T_K$. For temperatures much below $T/T_K = 0.5$, the equations are difficult to converge, while a thermal bias much below $\Delta T/T_K = 0.2$ results in a large signal to noise ratio in the procedure used to obtain I_{th} [see Eq.(S6)]. We therefore set $\Delta T/T_K = 0.2$. In Fig. S14 we show results for $T/T_K = 0.5$ (as in the main text) while in Fig. S15 we show the effect of using a higher temperature $T/T_K = 1.0$. One sees, that at the lower temperature, the same qualitative features are found as in the experiment, namely a kink in I_{th} vs V at high fields $B > T_K$ which is absent at low fields $B \ll T_K$. Upon increasing temperature, see Fig. S15, the kink is absent at high fields.

SM.3.6.4. Thermal bias dependence

The thermal bias dependence of I_{th} at two characteristic magnetic fields $g\mu_B B/k_B T_K = 0$ (i.e. at $B < B_c$) and $g\mu_B B/k_B T_K = 4$ (i.e., for $B > B_c$) is shown in Fig. S16 at a low base temperature $T/T_K = 0.5$ and in Fig. S17 at a higher base temperature $T/T_K = 1$. The top panels in each figure show I_{th} , while the bottom panels show $I_{\text{th}}/\Delta T$, where the latter representation brings out more clearly the evolution of the kink at $V = 0$ with thermal bias. The results at the lower base temperature and finite field, show more clearly the sign changes of the thermocurrent at low temperature and how these evolve (vanish) with increasing thermal bias. These results capture the main trends in the thermal-bias dependence of the experiments in Figs. S5a-b.

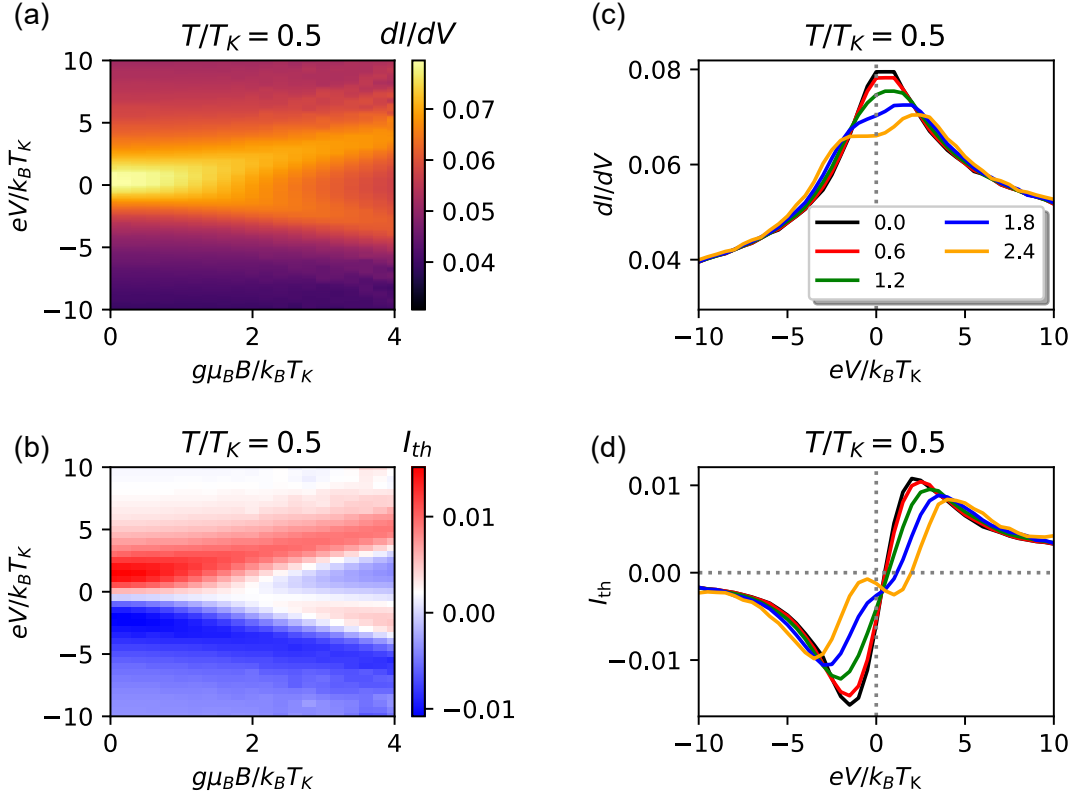


FIG. S14. Magnetic field dependence at low base temperature $T/T_K = 0.5$ and $\Delta T/T_K = 0.2$. (a),(c) Differential conductance vs bias voltage at different magnetic fields. (b),(d), Thermocurrent vs bias voltage at different magnetic fields. The linecuts in (c),(d) are for magnetic fields $g\mu_B B/k_B T_K$ indicated in the legend.

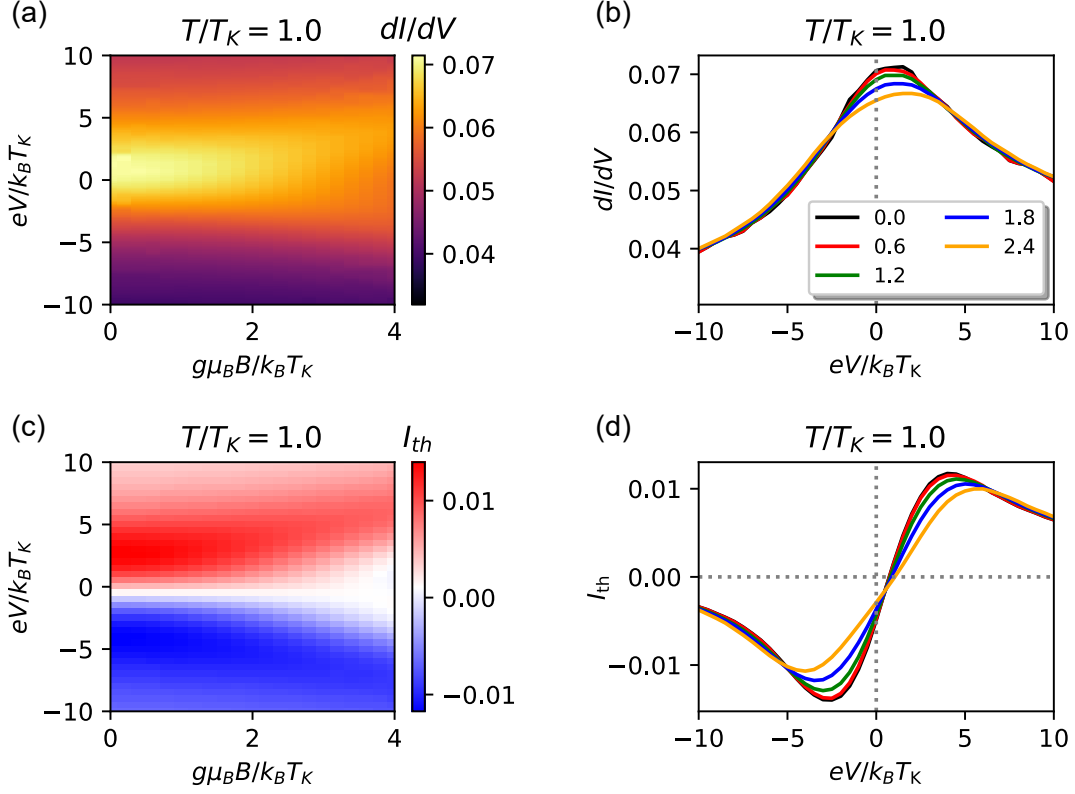


FIG. S15. Magnetic field dependence at higher base temperature $T/T_K = 1.0$ and $\Delta T/T_K = 0.2$. (a),(c) Differential conductance vs bias voltage at different magnetic fields. (b),(d), Thermocurrent vs bias voltage at different magnetic fields. The linecuts in (c),(d) are for magnetic fields $g\mu_B B/k_B T_K$ indicated in the legend.

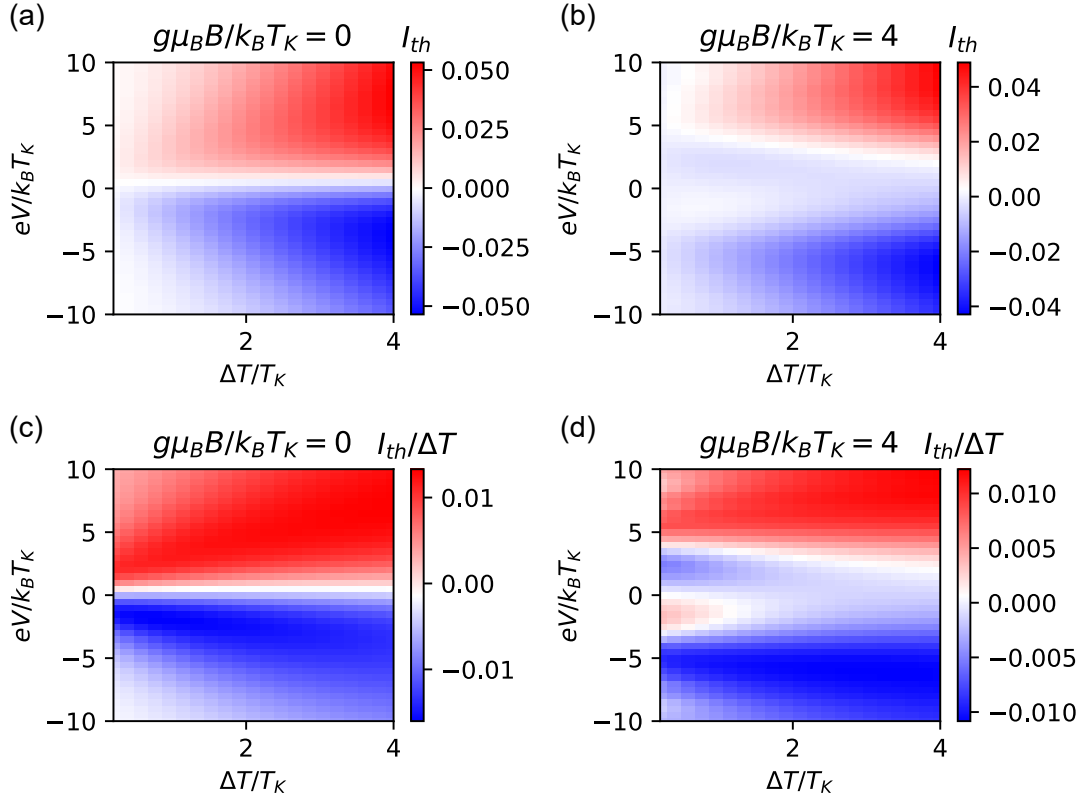


FIG. S16. Thermal bias dependence of the thermocurrent at low base temperature $T/T_K = 0.5$. Absolute thermocurrent I_{th} (top panels) and normalized thermocurrent $I_{th}/\Delta T$ (bottom panels) vs thermal bias $\Delta T/T_K$ and $eV/k_B T_K$ for $g\mu_B B/k_B T_K = 0$ (left panels) and $g\mu_B B/k_B T_K = 4$ (right panels).

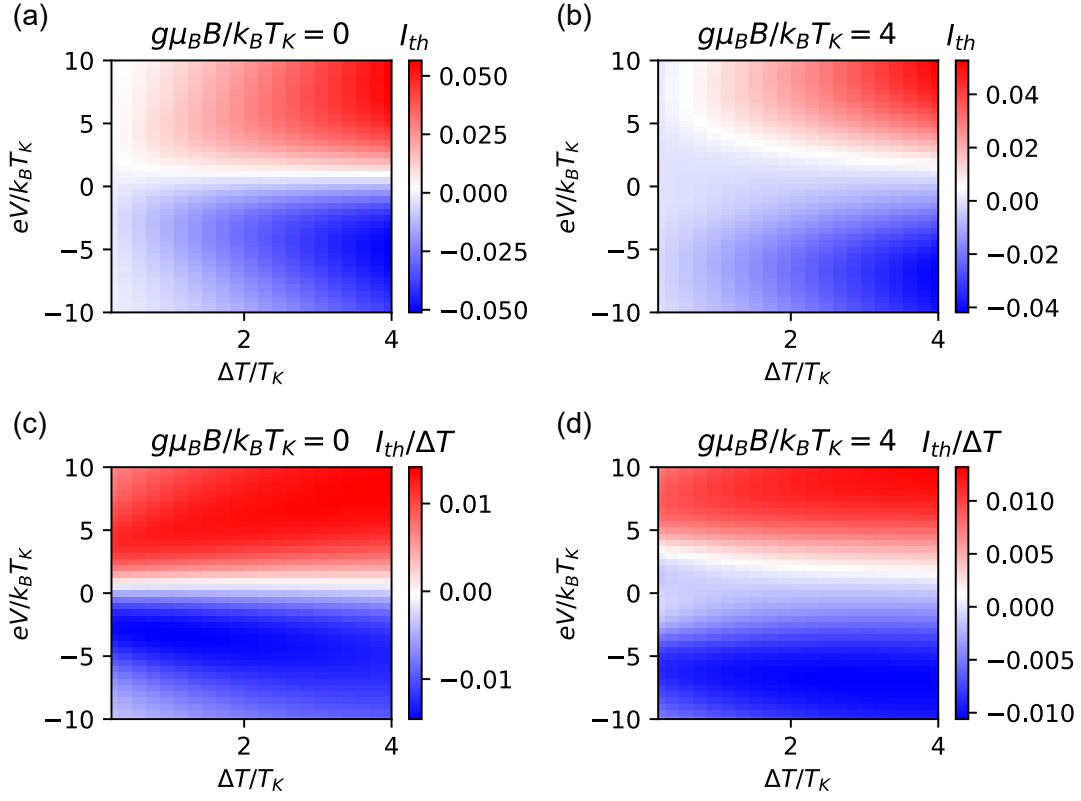


FIG. S17. Thermal bias dependence of the thermocurrent at a higher base temperature $T/T_K = 1.0$. Absolute thermocurrent I_{th} (top panels) and normalized thermocurrent $I_{th}/\Delta T$ (bottom panels) vs thermal bias $\Delta T/T_K$ and $eV/k_B T_K$ for $g\mu_B B/k_B T_K = 0$ (left panels) and $g\mu_B B/k_B T_K = 4$ (right panels).

SM.3.6.5. Temperature dependence

We show the temperature dependence of dI/dV and I_{th} in Fig. S18 for $g\mu_B B/k_B T_K = 0$ and $g\mu_B B/k_B T_K = 4$. A comparison for $B > B_c$ with the experimental data showed good qualitative agreement (see Fig.S4). In particular, the finite field thermocurrent for $B > T_K$ captures the feature seen in the experiment of an enhanced positive thermocurrent at low temperatures and $V < 0$.

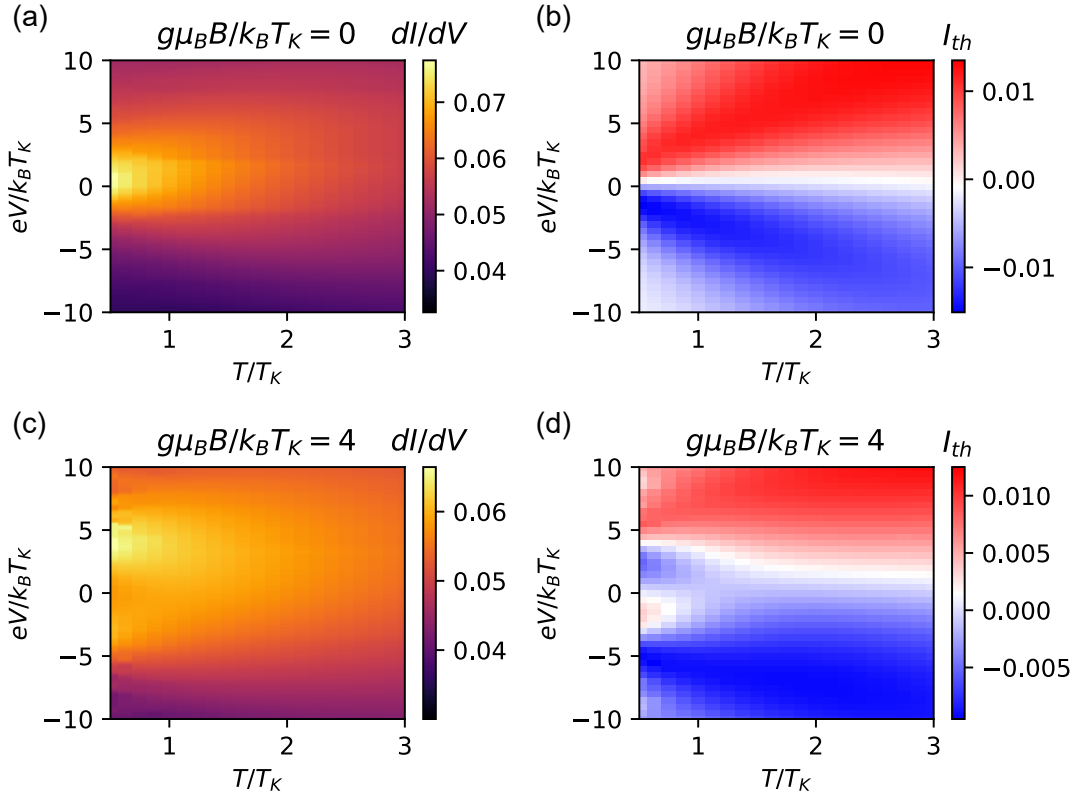


FIG. S18. Temperature and bias-voltage dependence of dI/dV (left panels) and I_{th} (right panels) at zero magnetic field $g\mu_B B/k_B T_K = 0$ (top panels) and at a high magnetic field $g\mu_B B/k_B T_K = 4$ (lower panels).

SM.3.6.6. Proportionality between I_{th} and d^2I/dV^2 at $\Delta T \ll T \ll T_K$

Finally, we comment briefly on the observed proportionality between I_{th} and d^2I/dV^2 seen experimentally for small $\Delta T \ll T \ll T_K$ in Fig. S2 at both zero and finite magnetic fields. For small bias voltage $V \ll T_K$, one can understand this within the higher-order Fermi-liquid theory of Sec. SM.3.5 as follows. From Eq. (S31), we have for $\Delta T \ll T \ll T_K$ and $V \ll T_K$, $d^2I/dV^2 \propto -\frac{c}{T_K} - 2c_V \frac{V}{T_K^2}$, while from Eq. (S18) we have that $I_{\text{th}}/\Delta T \propto T[s_0(B) + s_1(B)V]$, i.e., both I_{th} and d^2I/dV^2 are linear in V at low bias voltages, as also seen in the experiment in Fig. S2. The slopes with respect to V of I_{th} and d^2I/dV^2 are determined by the coefficients s_1 and c_V , respectively. These correlate as a function of field B as shown in Fig. S12 and Fig. S13(a). Moreover, these slopes both change sign at the same field $B \approx B_c$. Hence, the presence (for $B > B_c$) or absence (for $B < B_c$) of a kink in I_{th} at $V = 0$ correlates with the presence or absence of a similar kink in d^2I/dV^2 , as observed in Fig. S2. The above proportionality may be of practical use for detecting possible sign reversals of the zero-bias thermocurrent slope through purely electrical current measurements.

The proportionality between I_{th} and d^2I/dV^2 at $\Delta T \ll T \ll T_K$ extends, qualitatively, to larger voltages $V \gg T_K$, outside the regime of validity of the Fermi-liquid calculations. To access these voltages, we use the above equation of motion method (EOM). The results, shown in Fig. S19, show that a qualitative proportionality between I_{th} and d^2I/dV^2 extends to larger bias voltages, as observed experimentally in Fig. S2.

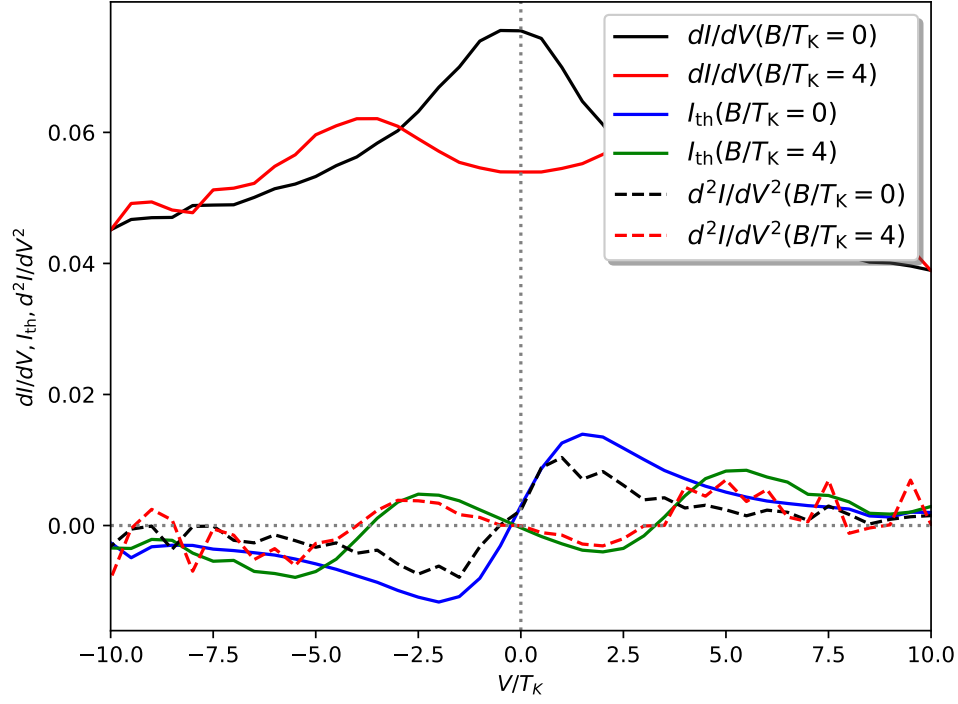


FIG. S19. Equation of motion method results showing the approximate proportionality between d^2I/dV^2 and I_{th} at $\Delta T \ll T \ll T_K$ for low and high magnetic fields and over a wide range of voltages. dI/dV is also shown. Parameters: $U = 8\Gamma$, $\varepsilon_0 = -3\Gamma$, $\Delta T/T_K = 0.2$, $T/T_K = 0.5$. Note the significant noise in the second numerical derivative of the current (d^2I/dV^2).

SM.4. SYNTHESIS & CHARACTERIZATION OF THE ORGANIC RADICAL

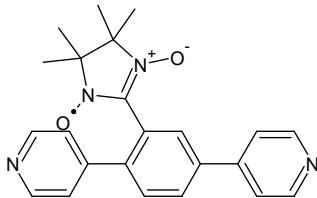


FIG. S20. Organic radical molecule with a backbone and a nitronyl-nitroxide side group where an unpaired electron resides.

In the experiment described in the main text and also here in the Supplemental information, an organic radical is used. The chemical structure of the organic radical is shown in Fig. S20, where an unpaired electron resides on a nitronyl-nitroxide side group. The structure of the molecule is very close to the previously reported Kondo-correlated system in STM [48], where a spin-1/2 Kondo effect was observed in the weak coupling regime. The radical in this letter has shorter pyridine anchoring sites, where the coupling between the electrodes and the unpaired electron is expected to be stronger. Confirmation is made based on the higher Kondo temperature T_K in our system, indicating our system is much stronger coupled.

SM.4.1. Synthesis

All chemicals and anhydrous solvents were used as purchased without further purification, unless stated otherwise. Deuterated solvents were obtained from Cambridge Isotope Laboratories, Inc. (Andover, MA, USA). All other commercial available starting materials were purchased from Sigma-Aldrich, Acros or Fluorochem. NMR experiments were acquired on a 400 or 500 MHz Bruker Avance III spectrometer equipped with a QNP or BBFO probe head respectively. The chemical shifts (δ) are reported in parts per million (ppm) relative to tetramethylsilane or referenced to residual solvent peaks and the J values are given in Hz (± 0.1 Hz). For high-resolution mass spectrometry (HRMS) a HR-ESI-ToF-MS measurement on a maXisTM 4G instrument from Bruker was performed. Column chromatography was performed on SiliaFlash® P60 from SILICYCLE with a particle size of 40-63 μm (230-400 mesh). Thin layer chromatography (TLC) was performed on Silica gel 60 F254 glass plates with a thickness of 0.25 mm from Merck using fluorescent quenching under UV light at 254 nm for the localization of sample spots. EPR spectra (X-band) were recorded on a Bruker ELEXSYS-II E500 CW-EPR spectrometer with attachment of a Bruker N₂ temperature controller. Samples for EPR measurements were prepared in capillary tubes. The software packages eview4wr and esimX were used for simulation [49]. UV-vis absorption spectra were recorded at 20 °C on a Jasco V-770 spectrophotometer. IR spectra were recorded with a Shimadzu IRTracer-100.

The synthesis of the nitronyl nitroxide radical (NNR) **1** was already reported elsewhere [50], and is summarized in Fig. S21. Starting from the commercially available 2,5-dibromobenzaldehyde, which was first protected as acetal **2** following a reported protocol [51]. A twofold *Suzuki* coupling with two equivalents of 4-pyridineboronic acid **3** followed by acidic deprotection yielded 2,5-di(pyridin-4-yl)benzaldehyde **5** in a good yield of 82% over three steps. The nitro compound **6** was converted to the hydroxyl amine **7** following a literature known procedure [52]. Condensation of the aldehyde **5** with the hydroxylamine **7** and successive in-situ oxidation with lead dioxide yielded NNR **1** in 36 % yield. The lead dioxide was freshly prepared from lead(IV) acetate as described by Wilmarth [53]. While scrutinizing the transport properties of NNR, G. V. Romanenko reported the synthesis of NNR, although by a different approach. The analytical data obtained by us matches the reported data of G.V.Romanenko [54]. Detailed experimental description and analytical details of

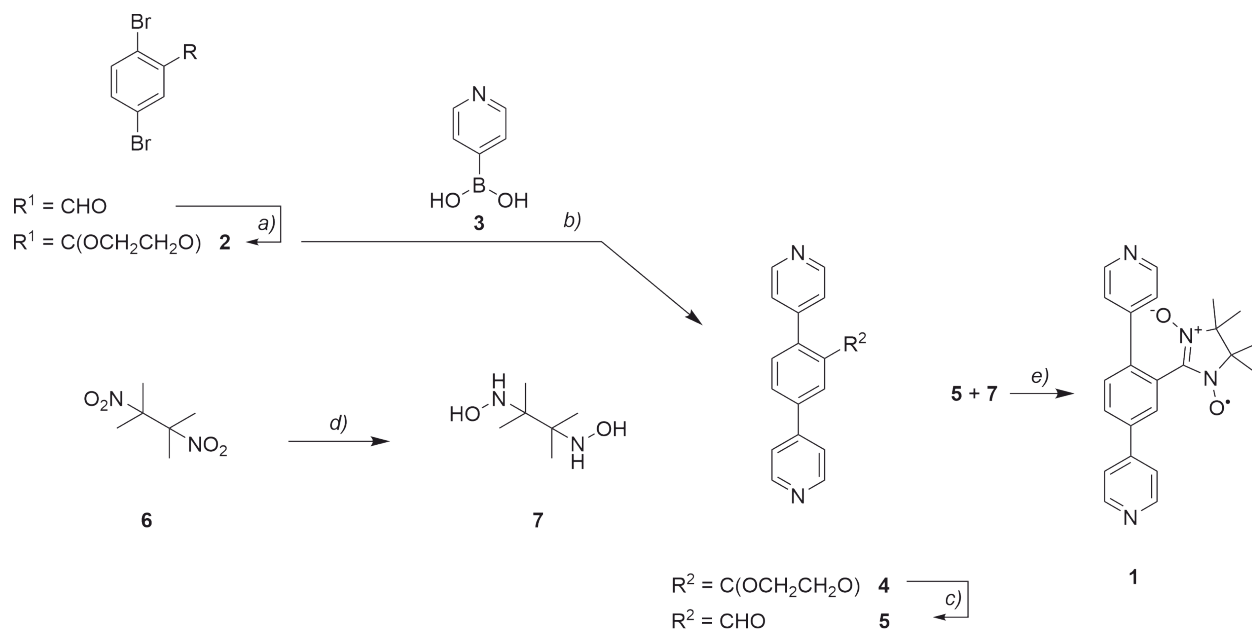


FIG. S21. Scheme 1: (a) TsOH, Toluene, dean-stark, reflux, quant. (b) $\text{Pd}(\text{PPh}_3)_2\text{Cl}_2$, K_2CO_3 , MeOH, Dioxane, 80 °C, 36 h, 90%, (c) 1 M HCl, THF, 1 h, r.t., 91%, (d), Zn, NH_4Cl , THF, H_2O , 0 - 10 °C, 48 h, 57%, (e) MeOH, PbO_2 , r.t., in the dark, 37 h, 36%

compounds **4**, **5** and **1** as well as cyclic voltammetry of **1** are published elsewhere [50].

**SM.4.2. Electron paramagnetic resonance spectroscopic analysis of the nitronyl
nitroxide Radical (NNR) 8**

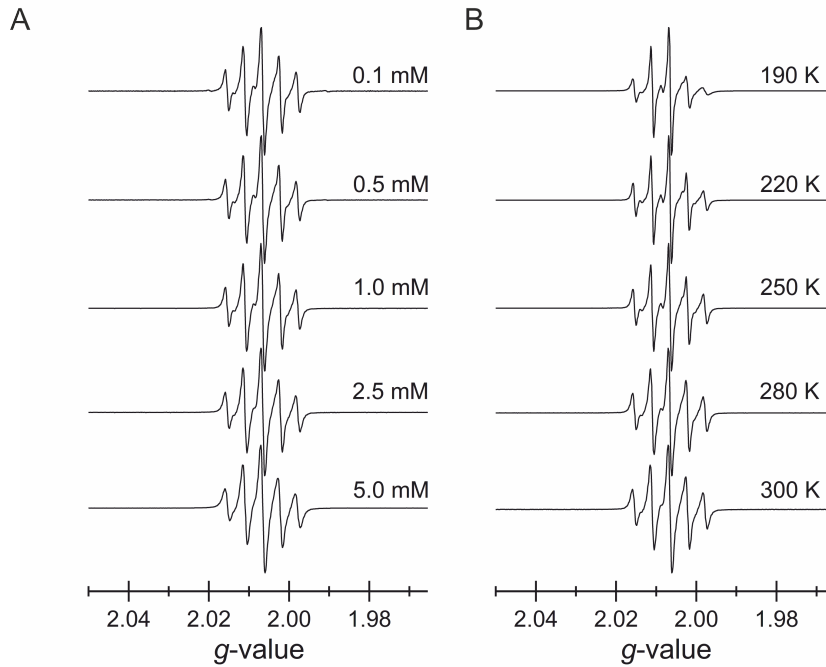


FIG. S22. (A) Concentration dependent EPR (X-band) spectra of NNR at 300 K, (B) Temperature dependent EPR (X-band) spectra of NNR (2.5 mM). All data was measured in DCM. Power attenuation: 25 dB. Microwave frequency: 9.45 GHz.

The EPR spectrum of NNR at 300 K (Fig. S22(A)) shows five lines of relative intensity 1:2:3:2:1 due to the coupling of the unpaired electron with two equivalent ^{14}N atoms ($I = 1$). The g -value is 2.0065 with a spacing of $a_{\text{N}} = 7.10$ G, which are normal parameters for nitronyl nitroxide monoradicals [55, 56]. There is no indication of a coupling to a third inequivalent ^{14}N atom demonstrating that the N atom of the *o*-pyridyl is too far away for interaction with the radical. With increasing concentration, the line shaping gets as expected

broadened, but the overall shape is relatively concentration independent. A splitting of the five lines in the EPR spectrum of NNR appears, when cooling the sample from 300 K to 190 K (Fig. S22(B)) along with line broadening and line asymmetry. At lower temperature the rotation around the phenyl-nitronyl nitroxide axis will be slowed down, hence resulting in inequivalence of the two N atoms in the nitronyl nitroxide unit. In agreement with our observations, the change from so-called “fast rotation” regime to “slow rotation” regime has previously been used to explain line broadening and asymmetric lines for nitronyl nitroxide monoradicals [57, 58].

-
- [1] H. Park, A. K. Lim, A. P. Alivisatos, J. Park, and P. L. McEuen, *Applied Physics Letters* **75**, 301 (1999).
 - [2] K. O'Neill, E. A. Osorio, and H. S. J. Van Der Zant, *Applied Physics Letters* **90**, 10.1063/1.2716989 (2007), arXiv:0702594 [cond-mat].
 - [3] P. Gehring, J. K. Sowa, C. Hsu, J. de Bruijkere, M. van der Star, J. J. Le Roy, L. Bogani, E. M. Gauger, and H. S. J. van der Zant, *Nature Nanotechnology* **16**, 426 (2021).
 - [4] P. Gehring, A. Harzheim, J. Spièce, Y. Sheng, G. Rogers, C. Evangeli, A. Mishra, B. J. Robinson, K. Porfyrakis, J. H. Warner, O. V. Kolosov, G. A. D. Briggs, and J. A. Mol, *Nano Letters* **17**, 7055 (2017).
 - [5] T. A. Costi, A. C. Hewson, and V. Zlatic, *Journal of Physics: Condensed Matter* **6**, 2519 (1994), arXiv:9310032 [cond-mat].
 - [6] D. Goldhaber-Gordon, J. Göres, M. A. Kastner, H. Shtrikman, D. Mahalu, and U. Meirav, *Physical Review Letters* **81**, 5225 (1998), arXiv:9807233 [cond-mat].
 - [7] A. Oguri and A. C. Hewson, *Phys. Rev. B* **97**, 035435 (2018).
 - [8] A. Oguri and A. C. Hewson, *Phys. Rev. Lett.* **120**, 126802 (2018).
 - [9] H. R. Krishna-murthy, J. W. Wilkins, and K. G. Wilson, *Phys. Rev. B* **21**, 1003 (1980).
 - [10] R. Bulla, T. A. Costi, and T. Pruschke, *Rev. Mod. Phys.* **80**, 395 (2008).
 - [11] R. Van Roermund, S.-y. Shiau, and M. Lavagna, *Physical Review B* **81**, 165115 (2010).
 - [12] M. Lavagna, *Journal of Physics: Conference Series* **592**, 012141 (2015).
 - [13] W. Hofstetter, *Phys. Rev. Lett.* **85**, 1508 (2000).
 - [14] R. Peters, T. Pruschke, and F. B. Anders, *Phys. Rev. B* **74**, 245114 (2006).
 - [15] A. Weichselbaum and J. von Delft, *Phys. Rev. Lett.* **99**, 076402 (2007).
 - [16] R. Bulla, A. C. Hewson, and T. Pruschke, *Journal of Physics: Condensed Matter* **10**, 8365 (1998).
 - [17] V. L. Campo and L. N. Oliveira, *Phys. Rev. B* **72**, 104432 (2005).
 - [18] A. C. Hewson, *The Kondo Problem to Heavy Fermions* (Cambridge University Press, Cambridge, 1997).
 - [19] T. A. Costi, *Phys. Rev. B* **100**, 161106 (2019).
 - [20] A. Rosch, T. A. Costi, J. Paaske, and P. Wölfle, *Phys. Rev. B* **68**, 014430 (2003).

- [21] L. Merker, S. Kirchner, E. Muñoz, and T. A. Costi, Phys. Rev. B **87**, 165132 (2013).
- [22] T. A. Costi, Physical Review Letters **85**, 1504 (2000), arXiv:0004302 [cond-mat].
- [23] M. Filippone, C. P. Moca, A. Weichselbaum, J. von Delft, and C. Mora, Phys. Rev. B **98**, 075404 (2018).
- [24] S. Hershfield, J. H. Davies, and J. W. Wilkins, Phys. Rev. B **46**, 7046 (1992).
- [25] Y. Meir and N. S. Wingreen, Phys. Rev. Lett. **68**, 2512 (1992).
- [26] A.-P. Jauho, N. S. Wingreen, and Y. Meir, Phys. Rev. B **50**, 5528 (1994).
- [27] The dependence of the dot spectral function on the thermal bias ΔT is implicit through the coupling of the dot to left and right reservoirs with temperature difference $T_L - T_R = \Delta T$.
- [28] T. Hata, Y. Teratani, T. Arakawa, S. Lee, M. Ferrier, R. Deblock, R. Sakano, A. Oguri, and K. Kobayashi, Nature Communications **12**, 3233 (2021).
- [29] P. Nozières, Journal of Low Temperature Physics **17**, 31 (1974).
- [30] C. Mora, C. P. Moca, J. von Delft, and G. Zaránd, Phys. Rev. B **92**, 075120 (2015).
- [31] This expression, for asymmetric couplings, has recently also been obtained in Ref. [59]. The general form of this expression is also known, but with approximate coefficients, from previous work [60, 61].
- [32] A. A. Aligia, P. Roura-Bas, and S. Florens, Phys. Rev. B **92**, 035404 (2015).
- [33] A. Kogan, S. Amasha, D. Goldhaber-Gordon, G. Granger, M. A. Kastner, and H. Shtrikman, Phys. Rev. Lett. **93**, 166602 (2004).
- [34] S. Amasha, I. J. Gelfand, M. A. Kastner, and A. Kogan, Phys. Rev. B **72**, 045308 (2005).
- [35] A. A. Houck, J. Labaziewicz, E. K. Chan, J. A. Folk, and I. L. Chuang, Nano Letters **5**, 1685 (2005), pMID: 16159205, <https://doi.org/10.1021/nl050799i>.
- [36] C. H. L. Quay, J. Cumings, S. J. Gamble, R. d. Picciotto, H. Kataura, and D. Goldhaber-Gordon, Phys. Rev. B **76**, 245311 (2007).
- [37] T.-M. Liu, B. Hemingway, A. Kogan, S. Herbert, and M. Melloch, Phys. Rev. Lett. **103**, 026803 (2009).
- [38] A. V. Kretinin, H. Shtrikman, D. Goldhaber-Gordon, M. Hanl, A. Weichselbaum, J. von Delft, T. Costi, and D. Mahalu, Phys. Rev. B **84**, 245316 (2011).
- [39] A. Svilans, M. Josefsson, A. M. Burke, S. Fahlvik, C. Thelander, H. Linke, and M. Leijnse, Physical Review Letters **121**, 206801 (2018), arXiv:1807.07807.
- [40] M. Yoshida, A. C. Seridonio, and L. N. Oliveira, Phys. Rev. B **80**, 235317 (2009).

- [41] T. A. Costi and V. Zlatić, Physical Review B - Condensed Matter and Materials Physics **81**, 235127 (2010).
- [42] C. Lacroix, Journal of Physics F: Metal Physics **11**, 2389 (1981).
- [43] U. Eckern and K. I. Wysokiński, New Journal of Physics **22**, 013045 (2020).
- [44] A related approach has been used to investigate the thermocurrent of a spin-1/2 quantum dot in the Kondo regime at zero bias voltage and zero magnetic field as a function of the thermal bias [62].
- [45] N. S. Wingreen and Y. Meir, Phys. Rev. B **49**, 11040 (1994).
- [46] We omit the dependence of the spectral function (and Green functions) on the thermal bias ΔT for simplicity of notation, but the dependence on this is implied.
- [47] Note that by “maintaining particle-hole symmetry” we do not imply that we are working at the special particle-hole symmetric point $\varepsilon_0 = -(\varepsilon_0 + U)$, i.e., at $\varepsilon_0 = -U/2$ (mid-valley). Instead, we are working at an arbitrary ε_0 and we symmetrize the results to ensure that the particle-hole transformation (symmetry) for the given ε_0 is satisfied.
- [48] Y. H. Zhang, S. Kahle, T. Herden, C. Stroh, M. Mayor, U. Schlickum, M. Ternes, P. Wahl, and K. Kern, Nature Communications **4**, 1 (2013).
- [49] B. Eckhard, (2016), max-Planck Institute for Chemical Energy Conservation, Mülheim, available from the author by mail on eckhard.bill@cec.mpg.de.
- [50] E. Pyurbeeva, C. Hsu, D. Vogel, C. Wegeberg, M. Mayor, H. van der Zant, J. A. Mol, and P. Gehring, Nano Letters **21**, 9715 (2021), arXiv:2109.06741.
- [51] J. L. Turnbull, B. R. Benlian, R. P. Golden, and E. W. Miller, Journal of the American Chemical Society **143**, 6194 (2021), publisher: American Chemical Society.
- [52] C. Hirel, K. E. Vostrikova, J. Pécaut, V. I. Ovcharenko, and P. Rey, Chemistry – A European Journal **7**, 2007 (2001).
- [53] W. K. Wilmarth and N. Schwartz, Journal of the American Chemical Society **77**, 4543 (1955), publisher: American Chemical Society.
- [54] G. V. Romanenko, S. V. Fokin, S. E. Tolstikov, G. A. Letyagin, A. S. Bogomyakov, and V. I. Ovcharenko, Journal of Structural Chemistry **61**, 906 (2020).
- [55] D. Wang, Y. Ma, B. Wolf, A. I. Kokorin, and M. Baumgarten, The Journal of Physical Chemistry A **122**, 574 (2018), publisher: American Chemical Society.
- [56] S. I. Zhivetyeva, I. A. Zayakin, I. Y. Bagryanskaya, E. V. Zaytseva, E. G. Bagryanskaya, and

- E. V. Tretyakov, *Tetrahedron* **74**, 3924 (2018).
- [57] T. J. Stone, T. Buckman, P. L. Nordio, and H. M. McConnell, *Proceedings of the National Academy of Sciences* **54**, 1010 (1965), publisher: National Academy of Sciences Section: Research Article.
- [58] V. Chechik, H. J. Wellsted, A. Korte, B. C. Gilbert, H. Caldararu, P. Ionita, and A. Caragheorghopol, *Faraday Discussions* **125**, 279 (2004), publisher: The Royal Society of Chemistry.
- [59] K. Tsutsumi, Y. Teratani, R. Sakano, and A. Oguri, *Phys. Rev. B* **104**, 235147 (2021).
- [60] E. Sela and J. Malecki, *Phys. Rev. B* **80**, 233103 (2009).
- [61] A. A. Aligia, *Journal of Physics: Condensed Matter* **24**, 015306 (2012).
- [62] M. A. Sierra, R. López, and D. Sánchez, *Phys. Rev. B* **96**, 085416 (2017).